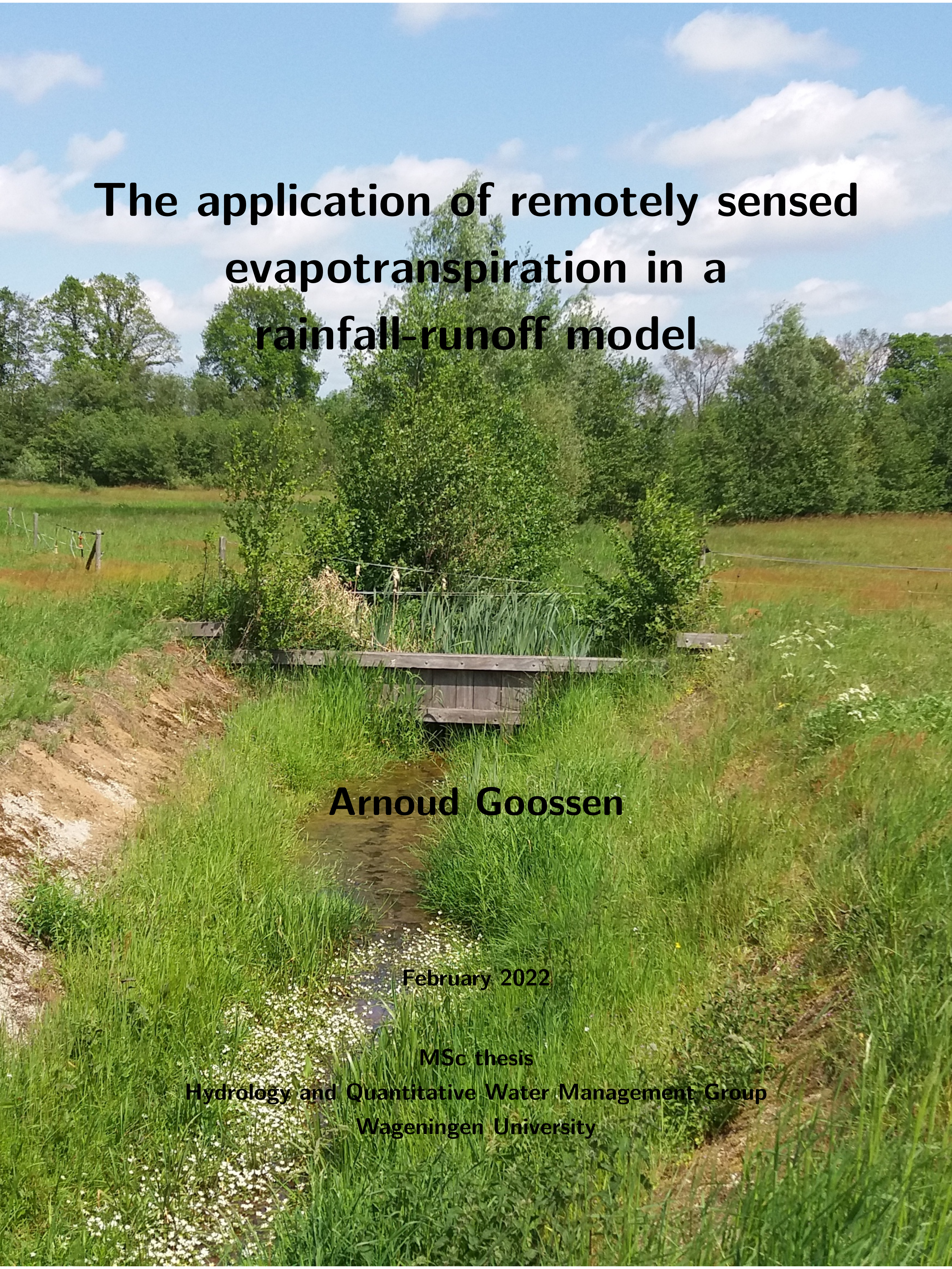

The application of remotely sensed evapotranspiration in a rainfall-runoff model

Arnoud Goossen

February 2022

MSc thesis
Hydrology and Quantitative Water Management Group
Wageningen University

The application of remotely sensed evapotranspiration in a rainfall-runoff model

MSc Thesis

Arnoud Goossen

Wageningen University & Research
Hydrology and Quantitative Water Management Group
MSc Earth & Environment
Date: February 2022
Supervisors:
Claudia Brauer & Martine van der Ploeg

Examinator:
Tim van Emmerik

Cover Image: The Hupsel Brook during excursion in June 2018. Photo made by Sjoerd Bezemer

Abstract

The Netherlands experienced many problems for water management and agriculture, as a consequence of recent droughts during summer. In this study, the effect of area-covering remotely sensed evapotranspiration as input in a rainfall-runoff model is analysed, to improve water management systems of Dutch water authorities. . The applicability of remotely sensed evapotranspiration (ET_{RS}) as input for the hydrological model WALRUS is analysed for three lowland catchments in the Netherlands (Hupsel Brook, Grote Waterleiding and Aa catchment). The quality of ET_{RS} was determined by comparing it with estimated reference evapotranspiration (by KNMI), potential evapotranspiration (including LULC) and actual evapotranspiration simulated by the hydrological model. ET_{RS} was significantly lower than the reference and potential evapotranspiration during periods without precipitation and higher than average temperatures, with a difference of ET-rates up to 2.5 mm/day. Spatial analysis of ET_{RS} showed significant spatial variability, however, no correlation was found with the land use land cover (LULC) in the catchments. Low discharges occurred during the growing season of 2020, due to ET losses up to 494 mm. The application of ET_{RS} had no significant influence on the discharge simulations, even though the estimated ET products differed significantly during the growing season of 2020. Due to the large spatial variability of ET_{RS}, further research is advised on the origin of the spatial variability.
Keywords: Evapotranspiration; Remote sensing; Lowland catchment; Hydrological model; WALRUS; Water balance

Contents

1 Introduction **1**

1.1 Thesis context 1

1.2 Research objective and questions 2

1.3 Thesis outline 2

2 Field site and data **3**

2.1 Catchments 3

2.2 Study period 5

2.3 Meteorological data 5

2.4 Discharge data 6

2.5 Land use 6

2.6 Climate 6

3 Methods **9**

3.1 Comparison of ET products 9

3.2 Analysis of spatial and temporal variability of ET_{RS} 10

3.3 Effect of land use on ET_{RS} 10

3.4 Hydrological model 10

4 Results **13**

4.1 Comparison of ET products 13

4.2 Spatial and temporal variability of RS ET 15

4.3 Land use 19

4.4 Hydrological model 19

5 Discussion **23**

5.1 Comparison of ET products 23

5.2 Spatial and temporal variability of RS ET 25

5.3 Land use 26

5.4 Hydrological model 27

6 Conclusion **29**

Acknowledgements **31**

Bibliography **33**

1 Introduction

1.1 Thesis context

The summer of 2018 in northwestern Europe was characterized by long-lasting large-scale high-pressure conditions, leading to dry and hot weather over large parts of the continent [Philip et al., 2020]. It is expected that as a result of global warming, similar weather conditions are more likely to occur in the future [Klein Tank et al., 2014]. According to the Dutch climate scenarios, for each degree in temperature increase, the potential evapotranspiration (ET_{pot}) rises by approximately 2% [Klein Tank et al., 2014]. As evapotranspiration (ET) is a large component in the hydrological balance, there is a demand for detailed and correct ET data for accurate rainfall-runoff modeling.

ET is defined as the total water vapor flux that leaves the system and includes the processes of soil evaporation, transpiration by plants, and evaporation of intercepted water [Moene and Van Dam, 2014]. The ET can be expressed as different concepts. In the Netherlands, the reference ET (ET_{ref}) is estimated by the Royal Dutch Meteorological Institute (KNMI) using in-situ measurements of global radiation and average daily temperature that are measured at 35 stations. Subsequently, the ET_{ref} is calculated with the Makkink equation [Makkink and Van Heemst, 1956], which estimates the ET of grass for Dutch summer conditions, without water stress [Moene and Van Dam, 2014]. A correction between the reference crop (i.e. grass) and crop to be investigated through a crop coefficient (K_c) results in the (ET_{pot}) [Bastiaanssen et al., 2005]. For applications which include possible water stress, a final hydrological reduction term is required to determine the actual ET (ET_{act}), which is assumed to be the real ET.

Instead of estimation methods of ET_{ref}, there are several methods that measure ET in-situ, such as the eddy-covariance method and lysimeters. However, the point-scale footprint of these in-situ measurements results in problems with heterogeneity, when applied to catchment scale [Armstrong et al., 2019]. Consequently, both the in-situ measurements, and the ET_{ref} estimated by KNMI can only show the spatial distribution through interpolation methods [Hiemstra and Sluiter, 2011]. Since the in-situ measurements of ET require a correction for vegetation types, a lack of surface vegetation information in rainfall-runoff modeling inputs may cause inaccurate estimates of water balance components, which decreases the performance of calibrated lumped rainfall-runoff models [Zhang et al., 2009].

With the rapid development of remote sensing (RS) technology, satellites and ET related products have gained increasing attention over the last decade (e.g. Wagle and Gowda [2019], Nouri et al. [2013]). The application of remotely sensed soil moisture data has already been widely applied in rainfall-runoff models, to improve discharge simulations. For example, Komma et al. [2008] and Alvarez-Garreton et al. [2014] proved that the use of assimilated soil moisture data improved flood forecasting in Austria and a semi-arid catchment in Australia.

In the Netherlands, steps have been made in applying remotely sensed data in operational water management, such as the OWAS1S-project (Optimizing Water Availability with Sentinel-1 Satellites). The project was initiated with the aim to investigate the possibilities of generating soil moisture maps with the integration of the Sentinel-1 data, and local knowledge on soil physical processes for optimizing water management of regional systems [Pezij et al., 2016].

In addition to RS soil moisture, numerous algorithms have been developed to estimate the ET based on satellite imagery (ET_{RS}) [Papadavid et al., 2013]. These methods are becoming attractive to estimate ET, as they cover large areas and can provide accurate and reliable estimates [Li et al., 2017]. Examples of such algorithms are SEBAL [Bastiaanssen et al., 1998], MODIS [Justice et al., 2002] and PROMET [Schneider, 2003]. Zhang et al. [2009] applied remotely sensed ET_{act} data for ungauged catchments in the southeast of Australia, which proved that remotely sensed data can further improve the prediction of runoff in ungauged catchments.

The water authorities in the east of the Netherlands have shown interest in the application of ET_{RS} in order to further improve their water management systems. However, no study has yet been conducted on the application of ET_{RS} as input of a rainfall-runoff model, to predict the discharge in catchments. The increasing occurrence of droughts during the growing season [Hari et al., 2020] poses new challenges for water authorities. High temperatures and low precipitation rates increase the demand for both domestic and agricultural (sprinkling) water usage. Simultaneously, the lack of precipitation during droughts leads to lower soil moisture contents, which results in decreasing ET_{act}. However, increasing ET_{act} patterns have also been noticed [Teuling et al., 2013].

In this study, the Wageningen Lowland Runoff Simulator (WALRUS) is used to simulate the rainfall-runoff process in the catchment of Hupsel Brook, Grote Waterleiding and the Aa. WALRUS is a lumped rainfall-runoff model, specifically developed for lowland catchments with shallow groundwater [Brauer et al., 2014a]. Normally, the ET_{pot} is used as input for the rainfall-runoff model. In this study, ET_{RS} is used as input to investigate whether this improves the performance of the rainfall-runoff model. The ET_{RS} product is distributed by VanderSat under the name of SatData 3.0. This product is also used to identify the effect of long periods of drought on ET_{act} and the resulting effect of increasing demand of water by agriculture for the use of irrigation.

1.2 Research objective and questions

The aim of this study is to identify the applicability of ET_{RS} in the rainfall-runoff model WALRUS, instead of the Makkink ET_{ref} estimated by KNMI. Different ET products are compared and used as input for WALRUS. In addition, spatial coverage of ET is used to acquire additional knowledge on the spatial variability on a catchment scale. The effect of land use on ET_{RS} is analysed in order to find patterns that describe the spatial variability of ET_{RS}.
Following from this research objective, the following main research question is formulated:

What is the effect of using area-covering ET_{RS} data as input for a rainfall-runoff model on the hydrological variables in a Dutch catchment?

In order to answer this question, the following sub-questions are formulated:

- ◇ How does the ET_{RS} compare with in-situ KNMI-measurements and WALRUS simulated ET_{act}.
- ◇ What is the spatial variability of ET_{RS}?
- ◇ What is the correlation between the spatial variation of ET_{RS} and land use?
- ◇ What is the effect of using ET_{RS} on the discharge- and groundwater simulations in WALRUS?

1.3 Thesis outline

Chapter 2 describes the study area, and characteristics of the three catchments. Also, the data sources and study period are defined, and a description of the climatic situation is given. In chapter 2.3, a detailed explanation on the methodologies is given. The results found in this study are given in chapter 4. The results are discussed in chapter 5, and linked with existing literature. The final conclusions and answers to the research questions are given in chapter 6.

2 | Field site and data

2.1 Catchments

The study area of this research consists of three lowland catchments in the Netherlands. Lowland catchments are defined as areas with shallow groundwater tables [Brauer et al., 2014a], of which the Hupsel Brook, Grote Waterleiding and the Aa are examples of lowland catchments. These catchments will be the focus of this study. Figure 2.1 illustrates the locations of the catchments in the Netherlands, and elevation profiles for each catchment.

The three catchments differ significantly in size, which is one of the reasons that these catchments are chosen. The size of a catchment influences the response time, which could result in different discharge responses during precipitation events. In addition, data availability was one of the criteria for the catchments. Meteorological measurements from a nearby KNMI station, as well discharge measurements have to be available for the study period.

Catchment	Area [km^2]	Discharge [m^{3}s^{-1}]
Hupsel	6.5	0.06
Grote Waterleiding	40.3	0.3
Aa	836	8.0

Table 2.1: The three catchments used in this study, with the surface area and yearly averaged discharge [WRIJ]

2.1.1 Hupsel Brook

The Hupsel Brook catchment is located in the east of the Netherlands near the villages Eibergen and Groenlo. The catchment has a surface area of 6.5 km^2, and is therefore the smallest catchment of the three. The elevations in the catchment vary between 22 and 35 m +MSL (see figure 2.1). The average slope in this catchment is 0.8%. The soil consists of a loamy sand layer of 0.2-10 m thickness on an impermeable clay layer of >20 m thickness [Brauer et al., 2018]. The catchment has a single outlet where all water discharges out of the area (see figure 2.1). The yearly average discharge at this outlet is 0.06 m^{3}s^{-1}. The land use is about 59% grassland, 23% maize, 3% forest, 2% built up, and 1% surface water [Brauer et al., 2018]. The remaining 12 % consist of infrastructure, grains, potato and the unclassified 'other' types. A map of the land use is illustrated in appendix .7a.

2.1.2 Grote Waterleiding

The catchment of Grote Waterleiding is also located in the east of the Netherlands, near the villages Lochem and Borculo. This catchment has a surface area of 40.3 km^2. The outlet of this catchment discharges into the Twentekanaal, with a yearly average discharge of 0.3 m^{3}s^{-1}. The river Berkel flows through the catchment, but there is only limited interaction occurs between the Berkel and Grote Waterleiding [WRIJ]. The Grote Waterleiding crosses the river Berkel through a sifon. In periods with low discharge, there is the possibility to let water in through the Horstgoot to prevent periods of no discharge [WRIJ]. Elevations in the catchment range from 11 to 50 m +MSL. The high elevations are located in the western part of the catchment, where the Lochemse berg is found. The average slope of the catchment is 0.5%. The soil consists mainly of loamy fine sand, which is similar to the Hupsel Brook catchment. The land use is about 62% grassland, 13% maize, 8% forest, 2% built up, and 0.5% surface water. The remaining 14 % consist of infrastructure, grains, potato, bush vegetation and the unclassified 'other' types. A map of the land use is illustrated in appendix .7b.

2.1.3 Aa

The Aa catchment is located in the province of North Brabant, and is with its surface area of 836 km^2 the largest of the three catchments (see Figure 2.1). The river Aa ends in Den Bosch, where it joins the river Dommel. North of Den Bosch, the water is discharged into the Meuse. The average discharge of the river Aa is around 8 m^{3}s^{-1}. The soil consists mainly of sand or loamy sands and the land surface is slightly sloping to the north-west. The land use in this catchment is mainly used for agricultural purposes [Versteeg et al., 2009]. Specifically, 27% is used as grasslands, 17% for maize, 12% is allocated to forest and nature reserves and 13% is built-up area. Surface water cover 1.4% of the catchment area. The remaining 30 % consist of infrastructure, grains, potato, bush vegetation, heather, peat and the unclassified 'other' types. A map of the land use is given in appendix .7c.

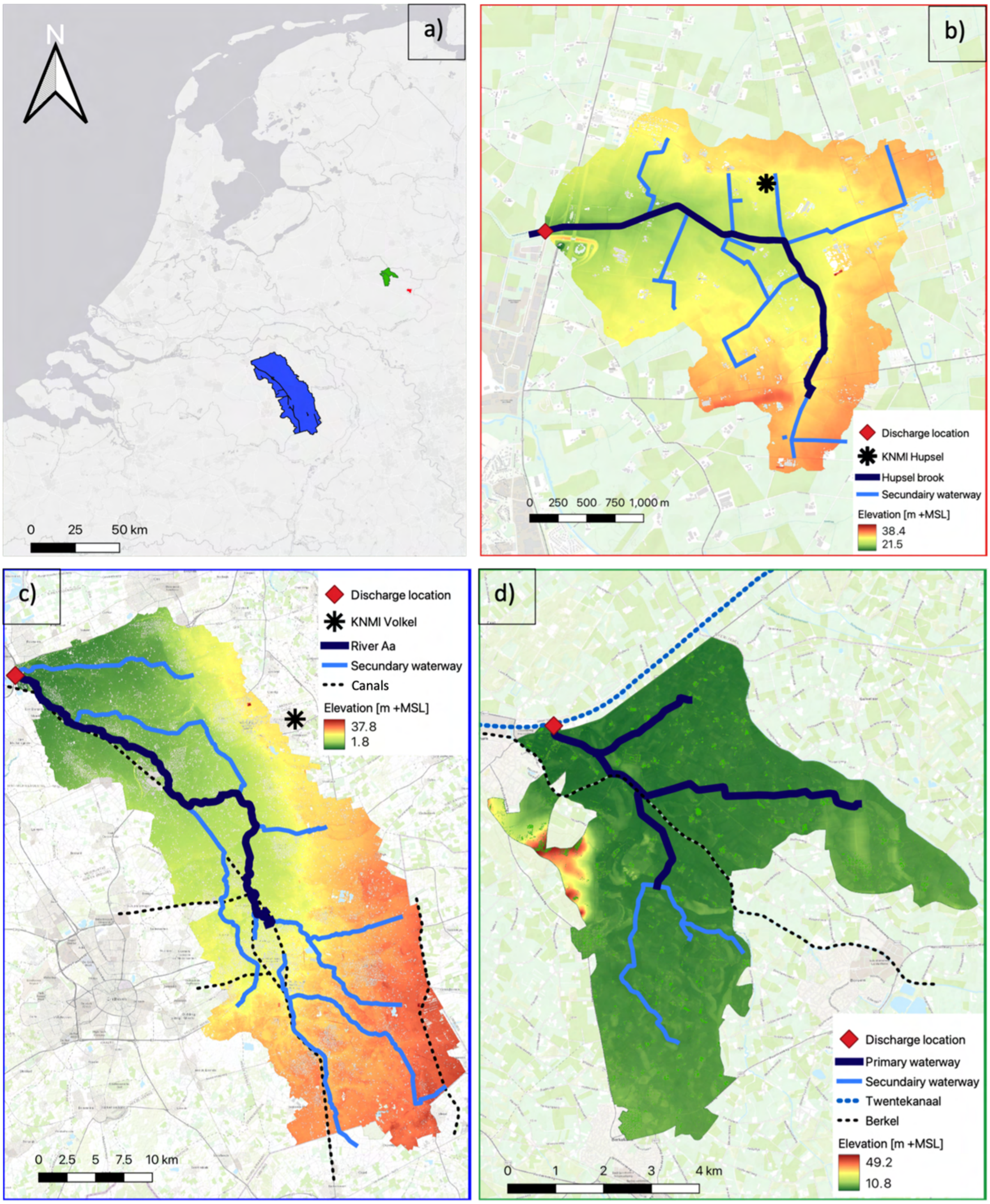

Figure 2.1: Visualisation of the study area; a) location of the three catchments in the Netherlands. The colors correspond to the three catchments: b) in red, the Hupsel Brook catchment, with KNMI weather station Hupsel inside the catchment. c) In blue, the river Aa catchment with KNMI station Volkel outside of the catchment. d) In green, the Grote Waterleiding catchment. The river Berkel flows through the catchment.

2.2 Study period

The growing season starts the 1st of April, and ends the 30th of September. It is generally known as the time period when the weather allows plants to grow. Increasing temperatures, combined with the growth of crops and vegetation, result in increasing ET-rates. Therefore, this period of the year is of special interest in this study.

2.3 Meteorological data

2.3.1 Weather stations

The Royal Netherlands Meteorological Institute (KNMI) manages 34 automatic weather stations in the Netherlands, which measure various variables with an hourly resolution [KNMI, 2021]. The meteorological data from KNMI station Hupsel is used for the catchment Hupsel Brook and Grote Waterleiding, and KNMI data from Volkel is used for the Aa catchment. Among the measured data, precipitation (P), reference evapotranspiration (ET_{ref}) for a well-watered reference grass, temperature (T) and global radiation (Q) time series are collected. P, T and Q are available in hourly time resolution. Daily ET_{ref} is aggregated to hourly resolution using hourly data of global radiation, which is further explained in section 3.1.1. Figure 2.2 gives the time series of P and T for the growing season of 2020.

2.3.2 Satellite data

In this study, a remotely sensed evapotranspiration (ET_{RS}) product will be used. This product is delivered by the company VanderSat in collaboration with the University of Gent, and gives insight in the ET_{act} of agricultural fields, urban areas, forests and open water [Vandersat]. The actual ET_{RS} is computed from a potential ET ($ET_{\text{pot,RS}}$) using a vegetation stress factor (S) and interception (ET_{int}) as equation 2.1.

$$ET_{\text{RS}} = ET_{\text{pot,RS}} \cdot S + ET_{\text{int}} \tag{2.1}$$

The product (ET_{RS}) used in this study originates from microwave satellite images with the relatively low spatial resolution of 25x25 km, which are scaled up to a higher spatial resolution of 100x100m. GLEAM (Global Land Evaporation Amsterdam Model) is a set of algorithms dedicated to the estimation of terrestrial evaporation and root-zone soil moisture from satellite data [Martens et al., 2017b]. GLEAM is used to model the ET_{RS} and uses the Priestley and Taylor [Priestley and TAYLOR, 1972] equation to calculate $ET_{\text{pot(RS)}}$, based on temperature and radiation observations [Martens et al., 2017a]. A brief description is given on the measurement requirements for the GLEAM model.

The radiation inputs are based on measurements from the Clouds and Earth's Radiant Energy System (CERES) on-board Terra and Aqua, which are globally available since the year 2001 on a 1 ° regular grid [Martens et al., 2017b]. Air temperatures are derived from measurements of the Atmospheric Infrared Sounder (AIRS), which are available since 2003, also on a global 1° regular grid [Martens et al., 2017b].

This $ET_{\text{pot(RS)}}$ is converted to actual ET_{RS}, by multiplying with a vegetation stress factor (S) [Martens et al., 2017a]. S is calculated as a function of microwave vegetation optical depth (VOD) and root-zone soil moisture [Martens et al., 2017a]. The microwave VOD is based on retrievals from passive microwave sensors using the Land Parameter Retrieval Model. The soil moisture data is retrieved from the SMOS Level 3 soil moisture produtct and the ESA Climate Change Initiative soil moisture dataset.

Lastly, the precipitation interception (ET_{int}) is based on the analytical model by Gash [1979]. The Tropical Rainfall Measurement Mission (TRMM) Multi-satellite Precipitation Analysis (TMPA) 3B42v7 product and the Multi-Source Weighted- Ensemble Precipitation (MSWEP) data set are selected, both with a spatial resolution of 0.25 °. For further details on the GLEAM model, is referred to Martens et al. [2017b] and Martens et al. [2018].

SatData upscaled the low resolution satellite images to a higher resolution of 100x100m. Subsequently, the GLEAM-HR (GLEAM High Resolution) runs for each 100x100m pixel. The latest version, SatData 3.0, recognizes four land use classfications based on Sentinel-2 optical satellite images; 1) high vegetation, 2) low vegetation, 3) Bare soil and 4) open water. Each pixel in the land use map contains fractions of each of these four classes, ranging from 0 to 100%. The land use map was created by aggregating 10m resolution Sentinel-2 optical satellite images to the GLEAM-HR resolution of 100x100m [Vandersat]. The fractions of the four land use classes are derived from the 100 sub-pixels in the high-resolution source files [Vandersat].

Finally, this results in the daily ET_{RS} that is used in this study. The final product, ET_{RS} is obtained via Meteobase [Meteobase]. In section 3.1, a more detailed explanation is given about the analysis of this data.

2.4 Discharge data

Discharge data is available with an hourly resolution. The discharge measurements from the outlets of the three catchments are collected. For the Hupsel Brook catchment and Grote Waterleiding, discharge is measured by water authority Rijn and IJssel [Waterschap Rijn en IJssel, 2021]. The discharge measurements stations for these catchments are respectively *Meetstuw Hupselse Beek - Overlaat* and *Debietmeting Grote Waterleiding*. The discharge of the Aa catchment is measured by the water authority of Aa and Maas. The discharge is measured at the location *ADM120 Oosterplas*.

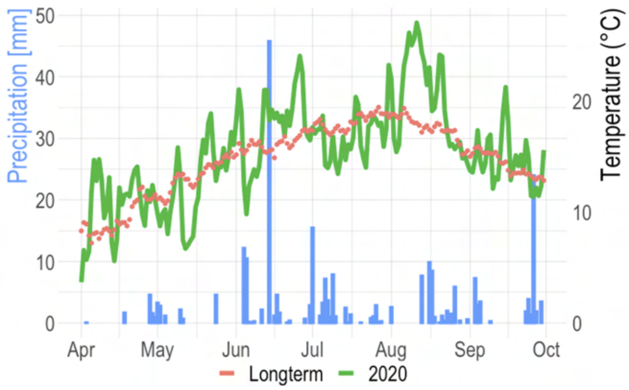

(a) KNMI Hupsel

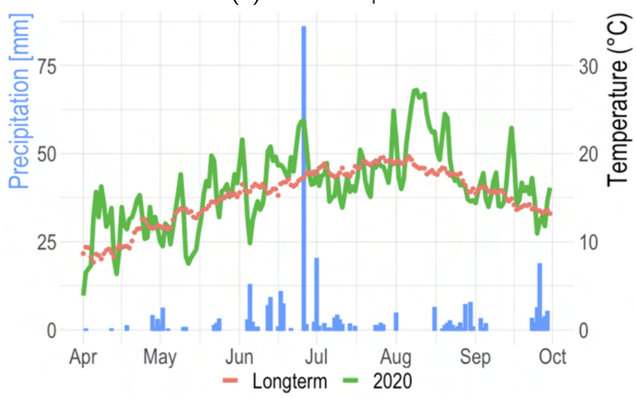

(b) KNMI Volkel

Figure 2.2: Temperature and precipitation in 2020 measured at the Hupsel and Volkel meteorological stations, and long-term (1991-2020) averaged T in red (dotted)

2.5 Land use

The ET_{RS} data gives insight in the spatial variability of ET, which can be compared and correlated with different types of land use. The newest version of the Landelijk Grondgebruik Nederland (LGN) will be used, namely LGN 2020. The resolution of this dataset is 25 x 25 m, and 48 land use types have been classified. The land use data is distributed via the Wageningen University (Geodesk). In this study, land use types are combined, and result in a total of 13 landuse classifications. In figure 2.3, the distribution of landuse types for each of the three catchments is illustrated. In Allen et al. [1998], the crop factor has been defined and calculated for different land use types. As explained in the introduction, the crop factor is used to calculate the ET_{pot}.

Table 2.2: Cumulative daily amount precipitation (P) and daily average temperature (T) during the growing season based on long-term (1991-2020) and the year 2020, measured at two KNMI-stations

KNMI station	P (long-term) [mm]	P (2020) [mm]
Hupsel	375.9	251.1
Volkel	363.5	287.8
	T (long-term) [°C]	T (2020) [°C]
Hupsel	14.9	15.5
Volkel	15.2	16.1

2.6 Climate

This study focuses on the growing season of 2020, which was relatively dry, especially the months April and May, in which a minimal amount of precipitation occurred (see figure 2.2). A comparison of the year 2020 has been made, with longterm precipitation and temperature data, to illustrate the dryness of the year 2020. This is illustrated in figure 2.4, where the longterm (1991-2020) cumulative daily averaged P is compared with the cumulative amount of daily P in the growing season of 2020, for KNMI Hupsel.

As already mentioned, the months April and May were notably dry. In April and May, the amount of P was respectively 9.0 and 10.6 mm, whereas the long-term average amount of P was respectively 38.7 and 52.6 mm. June 2020, on the contrary, was relatively wet due to heavy, local showers [KNMI, 2020]. However, the precipitation was unequally distributed throughout the Netherlands, which results in large variability in the amount of

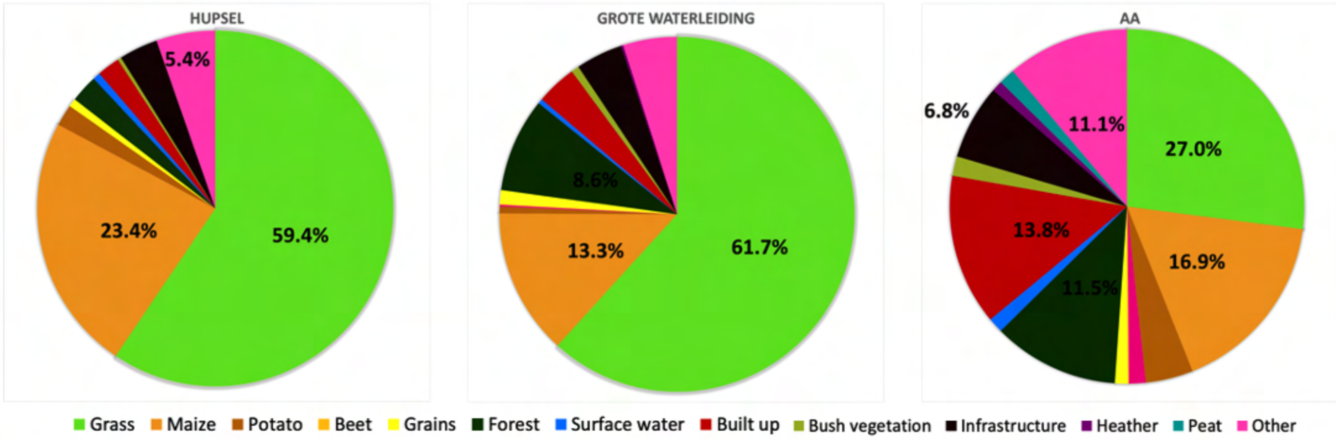

Figure 2.3: Distribution of the different land use types for the catchments Hupsel (left), Grote Waterleiding (center) and the Aa (right). The percentages higher then 5% are displayed in the piecharts.

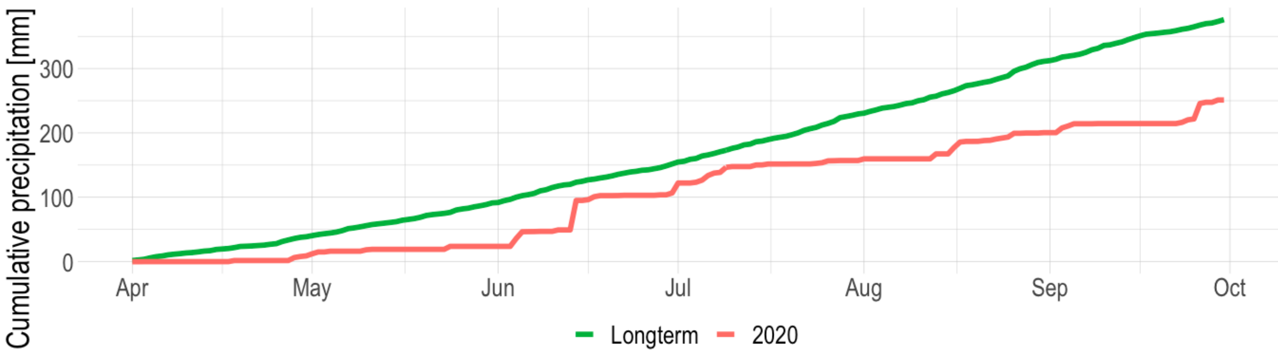

Figure 2.4: Cumulative daily averaged precipitation (in mm) measured at the Hupsel meteorological station, for long-term (in red) and for the year 2020 (in green)

rainfall in June. More specifically, the total amount of rainfall at KNMI Hupsel was 82.9, whereas KNMI Volkel measured a total of 142.2 mm. The months July, August and September had lower amounts of P than average. As a result, the total amount of P during the growing season of 2020 is significantly lower than average. A summary of the average values of P during the growing season is given in table 2.2.

The green line in figure 2.2 illustrates the daily averaged T at KNMI Hupsel (2.2a) and Volkel (2.2b), whereas the red dots illustrate the long-term averaged daily T. The month August draws special attention, as the Netherlands was experiencing a heat-wave from the 5th until the 18th of August. Overall, the temperatures during the growing season of 2020 were higher compared to the long-term averaged. In table 2.2, a summary of the average T values during the growing season is given.

3 Methods

This chapter covers the used data sources and the applied methods during this study. The study period is introduced, followed by the description of the different data sources. In section 2.6, the climatic conditions of the three catchments are discussed and compared with long-term (1991-2020) data. The methodology used to answer the research questions starts with section 3.1.

3.1 Comparison of ET products

3.1.1 Data preparation

The analysis of data starts with structuring and combining the different datasets. Hourly ET_{ref} rates are calculated with daily ET_{ref} measurements and global radiation, according to the following equation:

$$ET_{\text{ref,hour}} = \frac{ET_{\text{ref,hour}} \cdot Q^*_{\text{hour}}}{Q^*_{\text{day}}} \tag{3.1}$$

Here, Q^*_{hour} is the hourly global radiation (W/m^2) and Q^*_{day} is the daily total amount of global radiation (W/m^2). The $ET_{\text{ref,day}}$ is the daily amount of ET, as estimated by the KNMI, whereas the $ET_{\text{ref(hour)}}$ is the ET with an hourly resolution. From now on, whenever ET_{ref} is mentioned, it refers to ET_{ref} with hourly resolution. The ET_{pot} is required to analyze the effects of land use, and therefore a conversion from ET_{ref} to the ET_{pot} is needed. This conversion is performed with the crop factor (K_c), according to Allen et al. [1998]. The crop factors are derived from [Moene and Van Dam, 2014], and an overview is given in appendix .1. The calculation of ET_{pot} is given in the form of an equation as:

$$ET_{\text{pot}} = K_{\text{c}} \cdot ET_{\text{ref}} \tag{3.2}$$

The ET_{RS} data is collected for each catchment, via Meteobase [Meteobase]. The location of the boundary of each catchment is required to select the raster cells within the catchment boundary. As a result, the catchment average ET_{RS} is computed for each catchment. In order to obtain the catchment-average ET_{RS}, all ET_{RS} values per time-step are averaged.

Table 3.1: Overview of the ET products used in this study

ET-product	Estimation method	Spatial information
ET_{ref}	KNMI-station (Makkink)	no
ET_{pot}	KNMI + crop factor	no
$ET_{\text{act,sim}}$	WALRUS	no
ET_{RS}	Satellites + GLEAM(-HR)	yes

3.1.2 Evapotranspiration intercomparison

The ET_{ref} is subsequently calculated according to the Makkink equation [Makkink and Van Heemst, 1956]. RS techniques compute ET via algorithms from the energy balance equation, without further need to consider other complex hydrological processes, such as a correction for crop types (chapter 2.3). As a result, the error in the quantification is not propagated into ET [Mohamed et al., 2004]. However, the ET_{RS} is a product from the GLEAM(-HR) model, and thus, not a direct estimation method for ET. The different estimation approaches between in-situ, and RS estimations cause inequalities in the observations of ET. As differences between ET_{ref} and ET_{RS} can result from the fact that ET_{RS} is the estimated actual evapotranspiration, the ET_{RS} is also compared to the simulated ET_{act}. This $ET_{\text{act,sim}}$ is modelled in the hydrological model WALRUS, with ET_{pot} as input. Section 3.4 describes this process in more detail. An overview of the used ET products is given in table 3.1, describing the used estimation method and whether the product gives spatial information on catchment ET.

Statistical analysis

In order to identify the possible inequalities between the ET datasets, a statistical analysis is performed. First, four raster cells of 100x100 located above the KNMI meteorological weather stations are selected, and the resulting ET_{RS} data is collected. These ET_{RS} estimations are compared with the estimated ET_{ref} of the meteorological weather stations, to estimate the difference between the products, at a field of reference grass. After that, the four ET products are compared in time series. The summary statistics, i.e. mean, median, standard deviation, minimum and maximum, are collected and compared. Lastly, a linear regression analysis is performed. A linear model is created which compares the ET_{ref} with modelled $ET_{\text{act,sim}}$, and ET_{ref} with ET_{RS}. The descriptive statistics of this linear model give insight on the commonality of both measurement methods. It is, however, possible that certain influential points in the time series result in deterioration. Cook's Distance is a method to estimate the influence of data points when performing a least-square regression analysis [Cook, 1977]. The formula of Cook's Distance is given below:

$$D_i = \frac{\sum_{j=1}^{n}(\hat{y}_j - \hat{y}_{j(i)})^2}{ps^2} \tag{3.3}$$

Cook's distance D_i of observation i (for $i = 1, \ldots, n$) is defined as the sum of all the changes in the regression model when observation i is removed from it. Here, $\hat{y}_{j(i)}$ is the fitted response value obtained when excluding i, and s^2 is the mean squared error of the regression model.

3.2 Analysis of spatial and temporal variability of ET_{RS}

As KNMI estimates ET_{ref} in-situ, it is difficult to estimate the ET on a spatial scale. With ET_{RS}, however, estimates of ET are made for pixels of 100x100m, which offers the opportunity to calculate spatial variability of ET_{RS} on a catchment scale. Firstly, a basic statistical analysis is performed on the ET_{RS}, where the mean and standard deviation are calculated for each catchment during the growing season of 2020. Secondly, a geostatistical analysis is used to calculate the spatial dependence and variability of ET_{RS}. A semivariogram cloud is an important tool for investigating the spatial variability of the phenomenon under study [Gringarten and Deutsch, 2001]. Therefore, a semivariogram is produced, based on the semivariance of ET_{RS}, which is computed by:

$$\gamma(h) = 1/2[z(x_i) - z(x_j)]^2 \tag{3.4}$$

Here, $\gamma(h)$ is the semivariance, based on regionalized random variables ($z(x_i)$ and $z(x_j)$, for spatial positions x_i and x_j [Gringarten and Deutsch, 2001]. The semivariogram is fitted with an exponential model. This fitted semivariogram can be dissected into three elements: nugget, range, and sill. This results in a quantification of the spatial variation of ET_{RS}. The nugget-to-sill ratio describes the short-distance variation relative to the overall variation (sill). The spatial correlation length is described by the range.

3.3 Effect of land use on ET_{RS}

As explained in section 2.5, the LGN-dataset consists of 48 land use classifications. In this study, land use types are combined, and result in a total of 13 land use classifications. In figure 2.3, the distribution of land use types for each of the three catchments is illustrated. This distribution is required for estimating the ET_{pot}. Equation 3.2 describes how this ET_{pot} is calculated with the ET_{ref} and the crop factor (K_{c}). The crop factors are specifically used with the Makkink ET_{ref} for crops in the Netherlands, and is obtained from Moene and Van Dam [2014] (appendix .1). Clulow et al. [2015] determined the crop factors for peat in the Nkazana Peat Swamp Forest, South Africa. Although climatic conditions of that study are incomparable, these crop factor estimations have been used. The contribution of peat, built-up areas, heather, infrastructure and 'other' are minimal, as can be seen in figure 2.3. As no literature was found for built-up, infrastructure, and 'other', the Kc was estimated as 1.0 (see appendix .1).

3.4 Hydrological model

A significant part of this study focusses on the influence of different ET products on the performance of a hydrological model. In upcoming subsections, the input of the hydrological model WALRUS, and its simulations are discussed in more detail.

3.4.1 Model structure

WALRUS (Wageningen Lowland Runoff Simulator) is a lumped rainfall-runoff model that is specifically designed for application in lowland catchments and is designed by Brauer et al. [2014a]. WALRUS accounts for processes that are important for lowland catchments, which include; groundwater-unsaturated zone coupling, wetness-dependent flow routes, groundwater-surface water feedbacks, seepage and surface water supply [Brauer et al., 2014a]. The WALRUS model is suited for the three catchments, as the catchments satisfy the definition of lowland catchments (see chapter 2).

WALRUS consists of a coupled groundwater-vadose zone reservoir, a quickflow reservoir and a surface water reservoir. The saturated and unsaturated zone are coupled. A schematic overview of the model structure is given in figure 3.1. In the land surface compartment, P is divided between the different reservoirs. A fixed

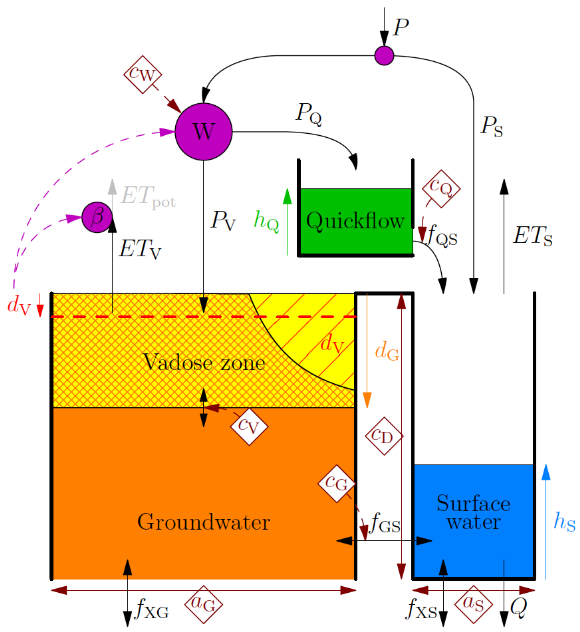

Figure 3.1: The model structure of WALRUS with the following compartments: a land surface (purple), a soil reservoir that consists of a vadose zone (yellow and red hatched) and a groundwater zone (orange), a quickflow reservoir (green) and a surface water reservoir (blue). Fluxes are black arrows, model parameters brown diamonds and the states are in the colour of the corresponding reservoir [Brauer et al., 2014a]

.

fraction is assigned to the surface water reservoir (P_S). The wetness index (W) determines the distribution of the remaining amount of P to the groundwater-vadose zone reservoir (P_V) and the quickflow reservoir (P_Q).

The groundwater-vadose zone reservoir consists out of the groundwater depth (d_G) and storage deficit (d_V) respectively. The groundwater table responds to changes in the unsaturated zone storage and determines, together with the surface water level, the amount of groundwater drainage or surface water infiltration (f_{GS}). The quickflow reservoir level (h_Q) determines the amount of water which will eventually be transported towards the surface water via quick flow routes (e.g. drain pipes, cracks in the soil). The water leaves the quickflow and groundwater-vadose zone reservoirs through evaporation and discharge by the surface water. The discharge is computed from the surface water level (h_S) via a $Q - h_S$-relationship. WALRUS requires parameter values and meteorological forcing in order to simulate discharge. Additionally, external fluxes can be implemented in the model. The parameters are time independent, whereas meteorological forcing and external fluxes vary in time.

3.4.2 Parameters

In order to run the model, hydrological properties of the catchments are required. In appendix .1, a table containing all the variables, parameters and functions in WALRUS is included. The parameter values are catchment specific. For optimizing discharge predictions, WALRUS requires calibration of three parameters: c_W (wetness index parameter), c_G (groundwater reservoir constant) and c_Q (quickflow reservoir constant). Parameters of the three catchments have already been estimated and calibrated in previous studies: Brauer et al. [2014b] for the Hupsel Brook, Heuvelink et al. [2020] for the Grote Waterleiding, and Gerritsen [2019] for the Aa. The calibrated parameters require special attention, as the focus on the growing season can impact certain parameters. In table 3.2, the parameters used in WALRUS are given for the three catchments. a_S is the surface water area fraction, c_D is the channel depth, c_S is the bankful discharge, c_V is the vadose zone relaxation time, and ST is the soil type.

3.4.3 Meteorological forcing

In section 2.3, the meteorological data that is used as input for the model is described. The initialization run (9 months) and model base run, uses ET_{pot} as input. The ET_{RS} model run, obviously, uses the ET_{RS} as input. In total, 9 model runs will be performed. An overview of the model runs is given in table 3.3, including the period of the model run, and which ET-product is used as input.

Normally, the ET_{act} in WALRUS is reduced based on simulated storage deficit. For this, an evapotranspiration reduction function is used, as described in Brauer et al. [2014a]. This evapotranspiration reduction function will be switched off when the ET_{RS} is used as input for the WALRUS model.

Table 3.3: Overview of the model runs performed in WALRUS. The initialization run considers the period January 1st - September 30th 2020, i.e. 9 months. The other two runs are performed over the growing season (GS) of 2020.

Period	Init. 9 months	Base run GS	ET_{RS} GS
Hupsel Brook	ET_{pot}	ET_{pot}	ET_{RS}
Grote Waterleiding	ET_{pot}	ET_{pot}	ET_{RS}
Aa	ET_{pot}	ET_{pot}	ET_{RS}

Table 3.2: WALRUS parameters for the three catchments. An extensive overview of the variables, functions and parameters is given in appendix .1

Catchment	Model parameters					Catchment characteristics			
	c_W [mm]	c_G [10^6 mm h]	c_Q [h]	c_V [h]	c_S [mmh^{-1}]	c_D [mm]	a_s [-]	Soil Type [-]	Size [km^2
Hupsel Brook	356	5	3	0.2	n.a.	1500	0.01	Hupsel	6.5
Grote Waterleiding	240	20	35	10	3	2200	0.01	loamy sand	40.3
Aa	350	30	85	10	6	2250	0.01	loamy sand	836

Table 3.4: Additional forcing for the three catchments. * only during the growing season, as stated by Gerritsen [2019]

Catchment	Additional forcing	
	f_{XG} [mmh^{-1}]	f_{XS} [mmh^{-1}]
Hupsel Brook	0	0
Grote Waterleiding	0	0.00912
Aa	0.015*	0.011

3.4.4 Surface water fluxes

The surface water fluxes are given in table 3.4. The channels and river flowing through the catchment of Grote Waterleiding and Aa influence the water balance. The fluxes are displayed in hourly resolution, as the model is performed with an hourly interval.

3.4.5 Initial conditions

The quickflow reservoir is initially empty. The initial surface water level is derived from the first discharge observation and the stage–discharge relation. For the Hupsel Brook catchment, the function that defines the stage-discharge relation is specifically defined, whereas for the other catchments the bankfull discharge (c_S) is given. As the focus in this study is on the growing season, the initial groundwater depth has to be computed for the first of April. The model is initialized with input data starting the 1st of January. The output file describes the values for each variable, where the dG_0, dV, hS and hQ are collected from. These values are used as the initial conditions.

3.4.6 Analysis

The output of the hydrological model consists of time series that illustrate the discharge (Q) and groundwater-levels. The course of these variables is visually inspected and compared. The performance of the hydrological model and the runs that are performed needs to be analysed. The simulated discharge is evaluated with the Nash-Sutcliffe Efficiency (NSE) [Nash and Sutcliffe, 1970], which is defined by:

$$NSE = 1 - \frac{\sum_{t=1}^{T}(Q^t_{sim} - Q^t_{obs})^2}{\sum_{t=1}^{T}(Q^t_{obs} - \bar{Q}_{obs})^2} \tag{3.5}$$

in which Q denotes the discharge at time step t, the subscripts mod and obs stand for modelled and observed. $\bar{Q}_{\text{obs}}$ represents the mean of the observed discharge, and T the number of discharge values. NSE values range between -∞ and 1. Values smaller than 0 indicate that the observed mean discharge is a better predictor than the simulated discharge and values higher than zero indicate the accuracy between the observed and simulated discharges, with 1 as the perfect match.

A second method to analyse the performance of the model, and to see whether ET_{RS} results in better estimates of Q is the water balance method. Ideally, the water balance equals 0, which means that incoming equals outgoing. In the form of an equation, this is as follows:

$$\Delta S = \sum P - \sum Q_{obs} - \sum ET + \sum f_{XG} + \sum f_{XS} \tag{3.6}$$

Here, the sum of rainfall (P), observed discharge (Q_{obs}), evapotranspiration (ET), seepage flux (f_{XG}) and water supply flux (f_{XS}) during the growing season are used. For ET, the different ET products can be used as input: ET_{ref}, ET_{pot} or the ET_{RS}.

4 | Results

In this chapter, the results of this study are illustrated. In section 4.1, the different ET products are compared. In section 4.2 the spatial and temporal variability of the remotely sensed ET product is analyzed. Section 4.3 focuses on the correlation between ET_{RS} and the different types of land use in the different catchments. Finally, the results on the hydrological modelling in WALRUS are described in section 4.4.

4.1 Comparison of ET products

A total of four ET products are discussed in this study; the ET_{ref} (calculated with Makkink), ET_{pot} (calculated with crop factors), ET_{act} (modelled in WALRUS) and ET_{RS} (ET_{act} modelled by VanderSat). As ET is largest during the growing season, the comparison is specifically performed for this period. First of all, the ET_{ref} is compared with the ET_{RS} raster data that are positioned above the KNMI measurement station. Four raster pixels are selected that are located above the measurement field. Table 4.1 illustrates the ET sum of the ET_{ref} and ET_{RS} of the field during the growing season of 2020.

The summed ET_{RS} was lower than the measured ET_{ref}. Table 4.1 shows that both methods result in a difference of 10.6% and 12.4% for KNMI Hupsel and KNMI Volkel, respectively. Whereas the ET_{ref} assumes well-watered conditions during the entire growing season, the ET_{RS} estimates the ET based on actual conditions and land use. In figure 4.1, box-plots are illustrated that compare the daily ET rates according to the different ET products for the Hupsel Brook catchment. The figures for the Grote Waterleiding and Aa catchment are similar, and therefore illustrated in the appendix (.2, .3). The daily average ET is lowest for ET_{act}, followed by ET_{RS}. Even though both ET_{act} and ET_{RS} consider both the different land use types and water availability,

Table 4.1: Comparison of ET during growing season in 2020 at two meteorological weather stations. ET_{ref} measured by KNMI and ET_{RS} is the remotely sensed ET product. Δ indicates the difference (%) of ET_{RS} relative to ET_{ref}

	ET_{ref} [mm]	ET_{RS} at KNMI station [mm]	Δ [%]
KNMI Hupsel	535	478	11
KNMI Volkel	564	494	12

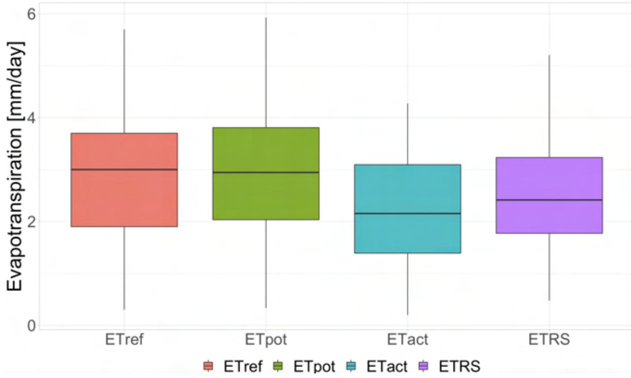

Figure 4.1: Comparison of daily ET rates according to different ET products, for the growing season of 2020.

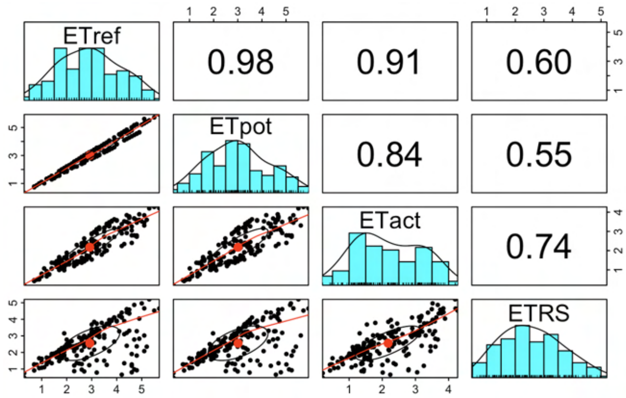

Figure 4.2: Correlation of the different ET products, for the Hupsel Brook catchment

the ET is not the same. For the Hupsel Brook, the average ET_{act} is 2.17 mm/day, whereas ET_{RS} averages to 2.55 mm/day. For the Hupsel Brook and Grote Waterleiding catchments, the difference between the daily average $ET_{\text{act,sim}}$ and ET_{RS} is respectively 0.38 mm/day and 0.37 mm/day, which summed up to 69.5 mm and 67.7 mm for the growing season of 2020. This means that the $ET_{\text{act,sim}}$ is lower compared to the ET_{RS}. For the Aa catchment, the ET_{RS} was lower, and the difference summed up to a difference of 20.1 mm.

Figure 4.2 illustrates pairwise scatter plots of all the variables as well as histograms, locally smoothed regressions, and the Pearson correlation, for the Hupsel Brook. The highest correlation ($\rho = 0.98$) is found between ET_{ref} and ET_{pot}. The highest correlation of ET_{RS} is found with ET_{act} ($\rho = 0.74$). Regardless that land use is included in the ET_{pot} through the crop factor, the lowest correlation is found between ET_{pot} and ET_{RS} ($\rho = 0.55$). The ellipse visualizes the values around the

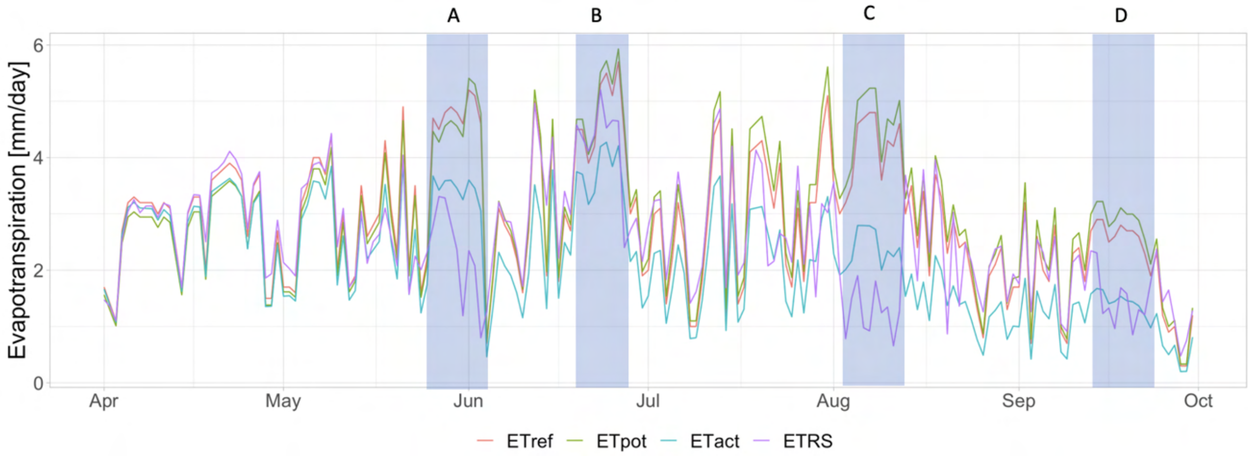

Figure 4.3: Time series of different ET products during the growing season of 2020, for the Hupsel Brook catchment

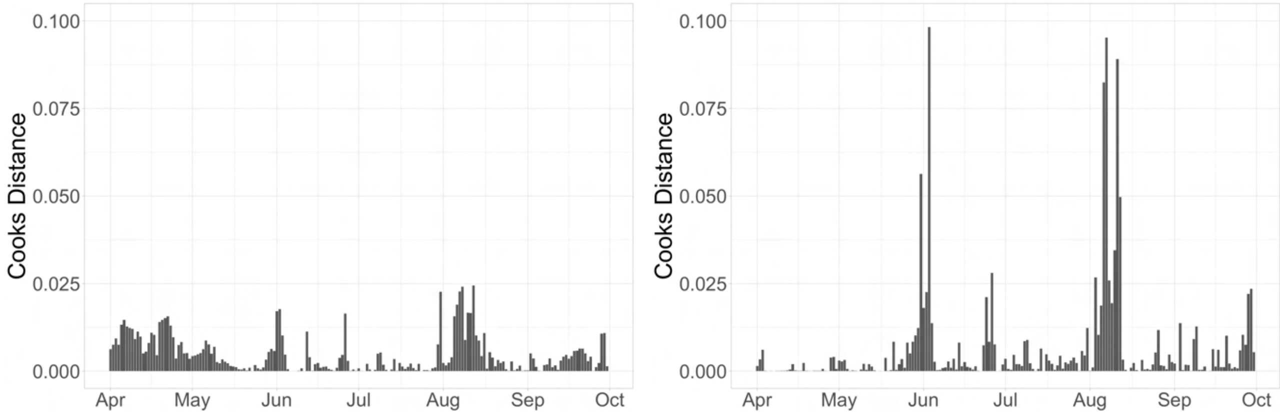

(a) linear model ET_{ref} vs ET_{act}

(b) linear model ET_{ref} vs ET_{RS}

Figure 4.4: Detection of influential points with Cooks Distance - Hupsel

mean with the axis length reflecting one standard deviation of the x and y variables, with red center dot illustrating the mean of both x and y variable. The scatter is highest for the comparisons with ET_{RS}, with a deflection downwards as ET-values become higher, especially for the comparison with ET_{ref} and ET_{pot}. These differences can be partly explained when considering the time-series of the ET products in figure 4.3.

In general, the four ET products follow a similar pattern throughout the growing season. However, there are four periods in which the difference between the ET is relatively large. These periods are highlighted in blue in figure 4.3. During these time spans, the ET_{act} and ET_{RS} behave differently, compared to ET_{ref} (and ET_{pot}). This is confirmed in figure 4.4, where the Cooks Distance is illustrated. This measure detects influential points in the regression model, as is described in more detail in section 3.1.2. The linear regression models that are assembled are ET_{ref} vs ET_{act} (figure 4.4a) and ET_{ref} vs ET_{RS} (figure 4.4b).

At the first view, figure 4.4a shows more scatter of the Cooks Distance values. However, the values are a factor four lower compared to the Cooks Distance in figure 4.4b. Significant influential points, i.e. points that strongly influence the fitted values, are detected in the period from the 25^{th} of May until the 4^{th} of June (period A), and the 2^{nd} until the 13^{th} of August (period C), mainly in figure 4.4b. Smaller peaks in the Cooks Distance are observed in the period of 19 until 26 June (period B) and the 10^{th} until the 24^{th} of September (period D). Accordingly, these periods or events are highlighted in figure 4.3.

Now that the periods are defined in which the ET products show significant differences, further analysis is required on the source of these differences. For this, the precipitation and temperature dataset is evaluated during the defined periods. In table 4.2, the total amount of rainfall, and the average and maximum temperature

Table 4.2: The amount of precipitation, average and maximum temperature for the periods where the ET products are different.

	Period	P [mm]	mean T [°C]	max T [°C]
A	25 May - 4 June	12.2	16.1	21.1
B	19 - 26 June	0.5	20.3	24.1
C	2 - 13 August	7.7	22.6	27.1
D	10-24 September	1.9	15.3	21.3

during the different time spans are given. The time series of temperature and precipitation events during the time spans is given in appendix .6. The graph with P and T during the growing season of 2020 can be found in figure 2.2, in section 2.6.

All periods are characterized by higher than average temperatures, and an increasing trend in the temperature. Besides that, little or no precipitation occurred during these periods. During period A and C, a precipitation amount of respectively 12.2mm and 7.7mm occurred at the end, after a period of dry and warm weather (table 4.2 and figure .6). Accordingly, the combination of a period without rainfall and high temperatures, result in a distinctive difference between the ET products. However, it is difficult to state whether one method or the other approaches the true ET, as the methods are based on assumptions and models. Therefore, a short analysis on the different responses of the products is performed.

In general, the ET_{ref}, ET_{pot} and ET_{act} follow the same pattern. The difference between ET_{ref} and ET_{pot} results from the crop factor (K_c), and both consider well-watered conditions. During the periods with higher than average T, and little or no P, the ET_{ref} and ET_{pot} estimate high ET-rates. This is also found in the time series in figure 4.3. The ET_{act} follows from the aforementioned ET products, however considers the conditions where deficiency of water could occur. This shortage of water is also taken into account in the ET_{RS}, although this product does not follow a similar pattern.

In period A and C, the ET_{RS} is lower than from the other methods. As the ET_{RS} is estimated using remotely sensed soil moisture images and surface temperatures, the low ET-values are therefore assumed to be the result of water deficiency in the topsoil, due to dry and warm weather conditions. Especially the ET_{RS}-product proves to be sensitive to such weather conditions. In upcoming sections, an analysis on whether this sensitivity has a significant impact on the modelling performance of a rainfall-runoff model is given.

4.2 Spatial and temporal variability of RS ET

In section 4.1, the results focused on temporal variability of the different ET products. For the ET_{RS}-product, the catchment average ET was used to illustrate the temporal variability in e.g. time-series. This section focuses on the analysis of the spatial variability of ET_{RS} during the growing season of 2020.

4.2.1 Spatial variability in the three catchments

The daily ET_{RS} of each raster cell resulted in basic statistics for the three catchments (see table 4.3). The numerical measures (mean, minimum, maximum, standard deviation) have been calculated by combining all raster cells, for all time steps, without averaging in space or time. The resulting standard deviation of the Hupsel Brook and Grote Waterleiding catchment are essentially the same (respectively, 0.272 versus 0.274), whereas the standard deviation is higher for the larger catchment Aa.

The ET_{RS} is estimated with a daily resolution. For each raster cell, the mean and standard deviation during the growing season of 2020 have been determined (figure 4.5 and 4.6). The catchment average ET_{RS} is respectively 2.55 mm/d for the Hupsel Brook, 2.70 mm/d for the Grote Waterleiding, and 2.51 mm/d for the Aa catchment (table 4.3).

4.2.2 Frequency distribution

Table 4.3 illustrated the catchment average and standard deviation (sd) of ET_{RS}. For each of the three catchments, a frequency distribution of the cell-averaged ET_{RS} (figure 4.7) and the sd of each raster cell during the growing season of 2020 (figure 4.8) was made.

The frequency distribution of ET_{RS} for the Aa catchment, follows an asymmetrical/bimodal distribution (figure 4.7c). The blue zones in figure 4.5c and 4.6c indicate significantly large areas where the average ET_{RS} is low, as well as low deviation. This is represented by the peak on the left of frequency distribution. The Hupsel Brook and Grote Waterleiding catchments have a frequency distribution that is skewed to the right (figure 4.7 & 4.8). The blue dashed line indicates the

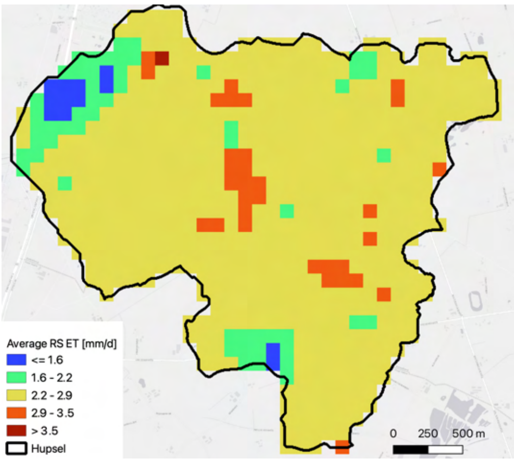

(a) Hupsel Brook

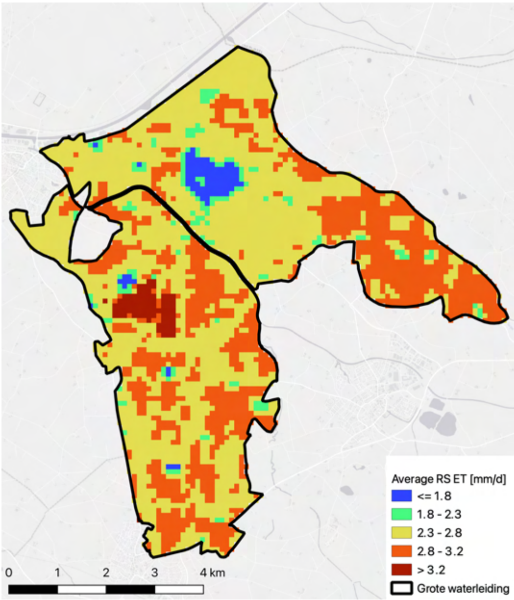

(b) Grote Waterleiding

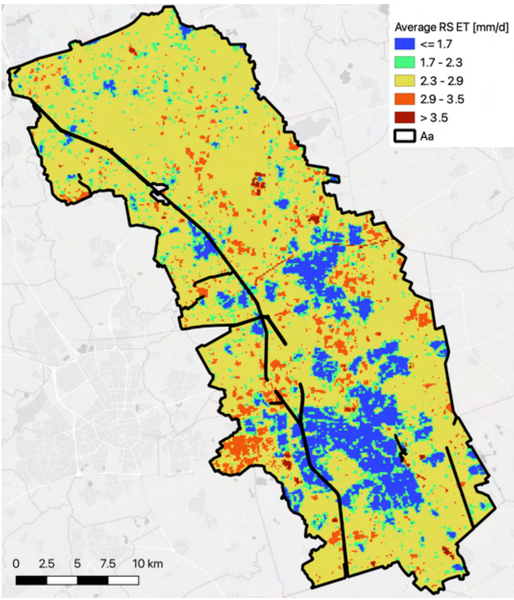

(c) Aa

Figure 4.5: The heterogeneity of daily average ET_{RS} during growing season of 2020

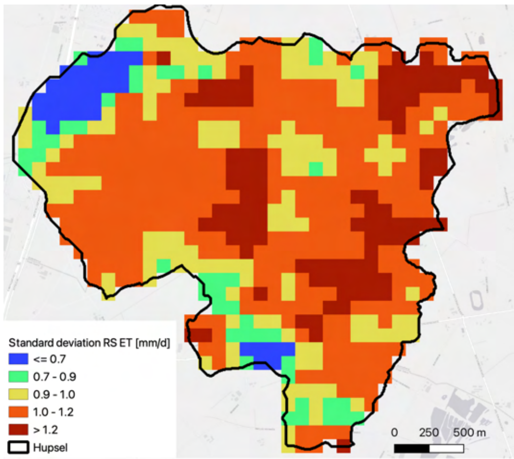

(a) Hupsel Brook

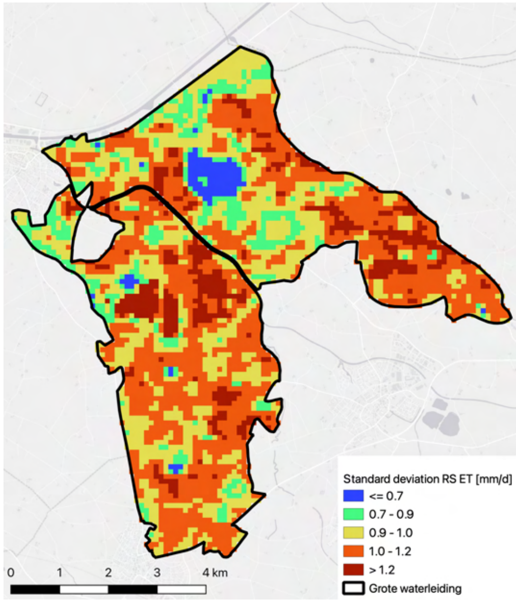

(b) Grote Waterleiding

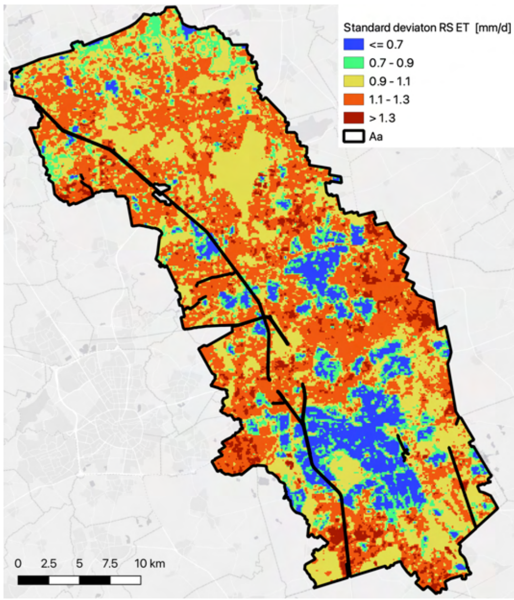

(c) Aa

Figure 4.6: The heterogeneity of the standard deviation of ET_{RS} during growing season of 2020

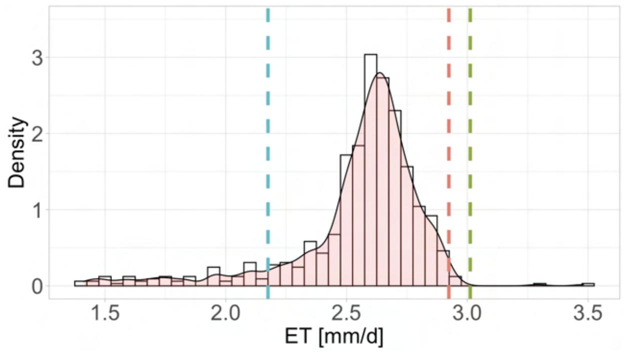

(a) Average ET_{RS} [mm/d], Hupsel Brook

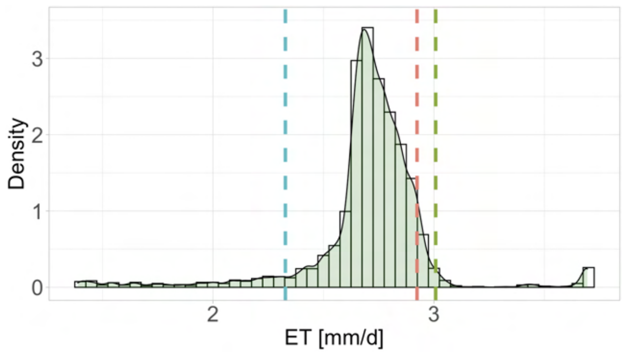

(b) Average ET_{RS} [mm/d], Grote Waterleiding

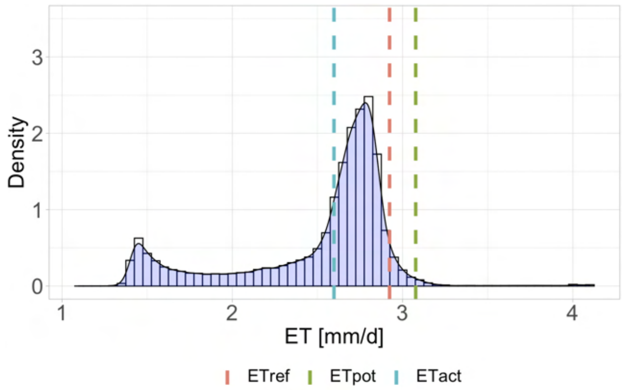

(c) Average ET_{RS} [mm/d], Aa

Figure 4.7: Frequency distribution of the average and standard deviation of ET_{RS} for the three catchments [mm/d]. The ET_{ref} is indicated with the blue dashed line

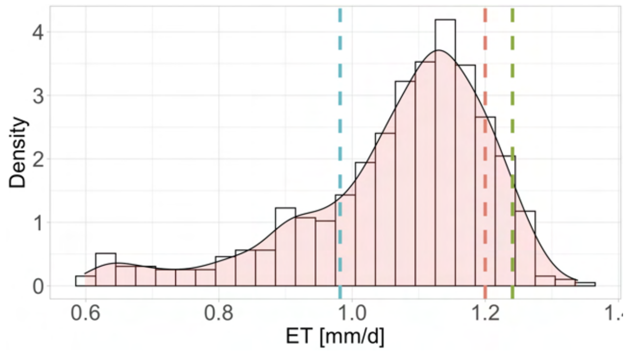

(a) Standard deviation of ET_{RS} [mm/d], Hupsel Brook

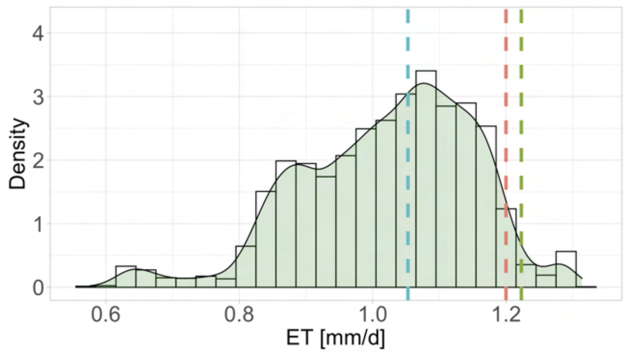

(b) Standard deviation of ET_{RS} [mm/d], Grote Waterleiding

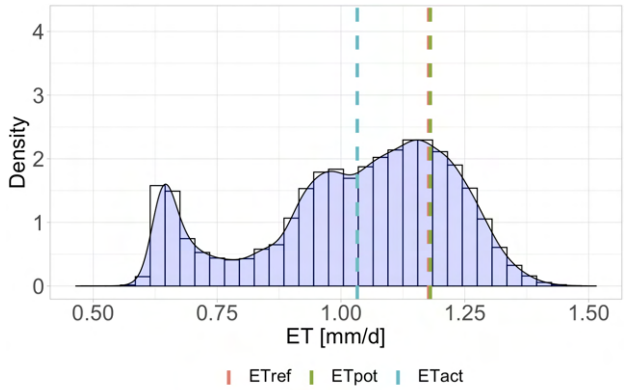

(c) Standard deviation of ET_{RS} [mm/d], Aa

Figure 4.8: Frequency distribution of the standard deviation of ET_{RS} for the three catchments [mm/d]. The ET_{ref} is indicated with the blue dashed line

average ET_{ref} estimated by KNMI for the growing season of 2020. As already stated in section 4.1, the ET_{ref} is on average higher than the ET_{RS}.

4.2.3 Geo-statistical analysis

If ET_{RS} is spatially dependent, then pairs of points that are closer in distance will have more similar values than pairs that are farther apart. In other words, the semivariance is expected to increase as the distance increase. This phenomenon is illustrated by a semivariogram (figure 4.9). The points in figure 4.9 represent the experimental semivariogram, whereas the solid line is the fitted exponential semivariogram model. The x-axis represents the geographical distance (m), and the y-axis represents the semivariance ($\mathrm{mm}^2/\mathrm{d}^2$). The nugget, sill and range are a result of the fitted exponential semivariogram. These elements have been calculated for the three catchments based on the fitted exponential model (see table 4.4). The standard deviation (sd_{sill}) is calculated by taking the square-root of the sill. The sd_{calc} is the calculated standard deviation from section 4.2.1. The standard deviations have similar values, which means that the fitted exponential model managed to represent the

Table 4.3: Basic statistics of spatial variability during the growing season of 2020

Catchment	Mean (μ) [mm/d]	min [mm/d]	max [mm/d]	sd (σ) [mm/d]
Hupsel	2.55	1.41	3.48	0.27
Grote Waterleiding	2.70	1.39	3.69	0.27
Aa	2.51	1.09	4.09	0.46

Table 4.4: The geostatistical elements of the semivariograms for the three catchments, based on average ET_{RS} and standard deviation of ET_{RS}

		Nugget	Partial sill	Sill	Range	Nugget-Sill ratio	sd_{sill}	sd_{calc}
Hupsel	Average	0.00	0.07	0.07	359.94	0.00	0.27	0.27
	SD	0.00	0.02	0.02	374.17	0.00		
Grote Waterleiding	Average	0.00	0.09	0.09	477.49	0.00	0.30	0.27
	SD	0.00	0.02	0.02	434.59	0.05		
Aa	Average	0.05	0.17	0.22	1724.82	0.24	0.47	0.46
	SD	0.01	0.03	0.04	2036.53	0.28		

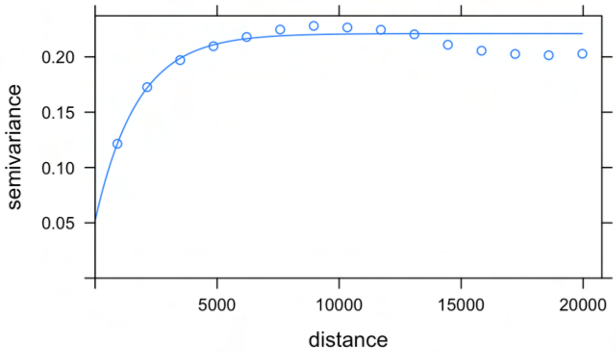

Figure 4.9: Experimental semivariogram and fitted exponential semivariogram model of average ET_{RS} for the Aa catchment

spatial variability. An overview of the six semivariograms can be found in appendix .8

4.2.4 Spatial variability during periods of interest

In section 4.1, four periods have been defined where the ET_{RS} was significantly lower than ET_{ref}. The analysis illustrated that all periods were lacking precipitation, and the temperatures were high. Therefore, these four periods require additional interest, to check whether the lower than average ET is a result of e.g. outliers. The average ET_{RS} and the standard deviation have been plotted for the Hupsel Brook catchment during period A (25 May - 4 June) (figure 4.10). The range of the values is similar to figures 4.5a and 4.6a. The figures concerning the other periods of the Hupsel Brook catchment are illustrated in appendix .9.

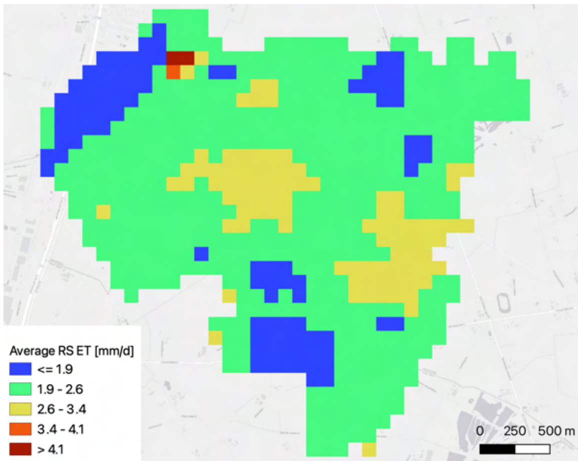

(a) Average ET_{RS} [mm/d] during Period A for the Hupsel Brook catchment

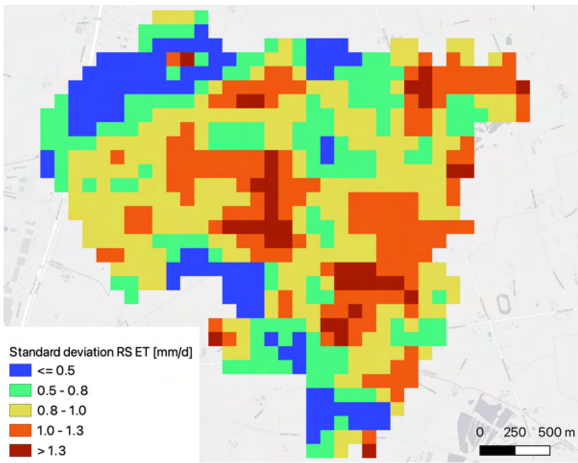

(b) Standard deviation of ET_{RS} [mm/d] during Period A for the Hupsel Brook catchment

Figure 4.10: Average and standard deviation of ET_{RS} [mm/d] during period A

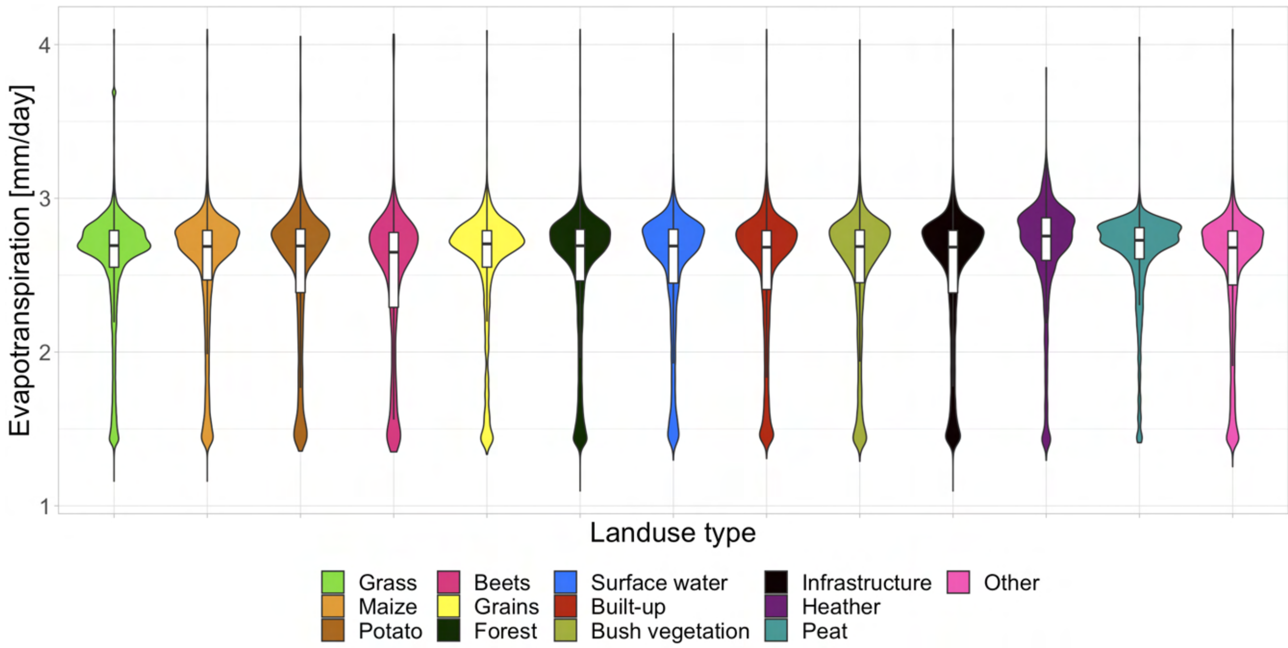

Figure 4.11: Violin plot illustrating the distribution ET_{RS} for each land use classification. The boxplots (in white) shows the median, 25th and 75th Percentile of the ET_{RS} per landuse

4.3 Land use

Different types of crops, vegetation, or land use in general, influence the amount of ET. Therefore, an analysis has been performed on the correlation between land use types and amount of ET_{RS}. The land use maps are given in the appendix .7. The analysis resulted in basic statistics about the ET_{RS} per type of land use (table (appendix)). The resulting distribution of ET_{RS} is illustrated for each land use type in the violin plot (figure 4.11).

4.4 Hydrological model

This part is about the hydrological modelling in WALRUS. In total, 9 model runs have been performed, consisting of three runs per catchment. The base run of 9 months started at January 1st, and lasts until the last day of September. This model run is used to define the initial groundwater level (dG_0), dV, hS and hQ for the three catchments on the 1st of April 2020. This resulted in groundwater levels of 1.26, 1.27 and 1.38 m below surface level for the Hupsel Brook, Grote Waterleiding and Aa catchments respectively. The other model runs (respectively Base run (g.s.) and ET_{RS}) have been performed on the period of the growing season (g.s.) 2020. The ET_{RS} model run has been performed with the remotely sensed ET data as input.

Table 4.6: The Nash-Sutcliffe Efficiencies of the 9 discharge simulations. The initialization run started the 1st of January 2020, whereas the base run (g.s.) and ET_{RS} model runs are during the growing season of 2020. G.s. indicates growing season

NSE	Init.	Base run (g.s.)	ET_{RS}
Hupsel	0.54	0.26	0.10
Grote Waterleiding	0.34	-3.11	-2.95
Aa	0.76	-0.15	-0.58

The WALRUS model runs result in different simulations of the various variables. In this study, the focus was on the effect of using ET_{RS} as input of the hydrological model, on both discharge and groundwater simulations. The simulations of discharge and groundwater levels during the growing season are given for the three catchments. Figure 4.12 illustrates the response of discharge on the precipitation events during the growing season of 2020. The simulated discharge for the base run is given in red, and the simulation with ET_{RS} input data is given in blue. The actual discharge, i.e. observed discharge, is given in green. Similarly, the groundwater simulation for the Grote Waterleiding is illustrated (figure 4.12b). As a result of higher ET rates during the growing season of 2020, the groundwater-levels gradually decrease. The daily summed precipitation shows that certain amount of rainfall result in changes of groundwater-level. From the figure, the groundwater-level according to the modelled base run and ET_{RS} simulation can be compared.

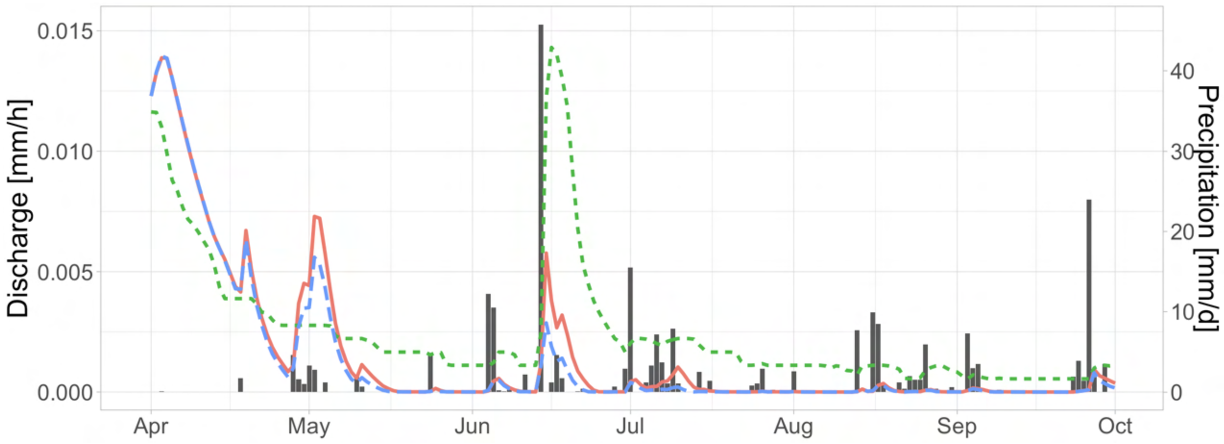

(a) Hupsel

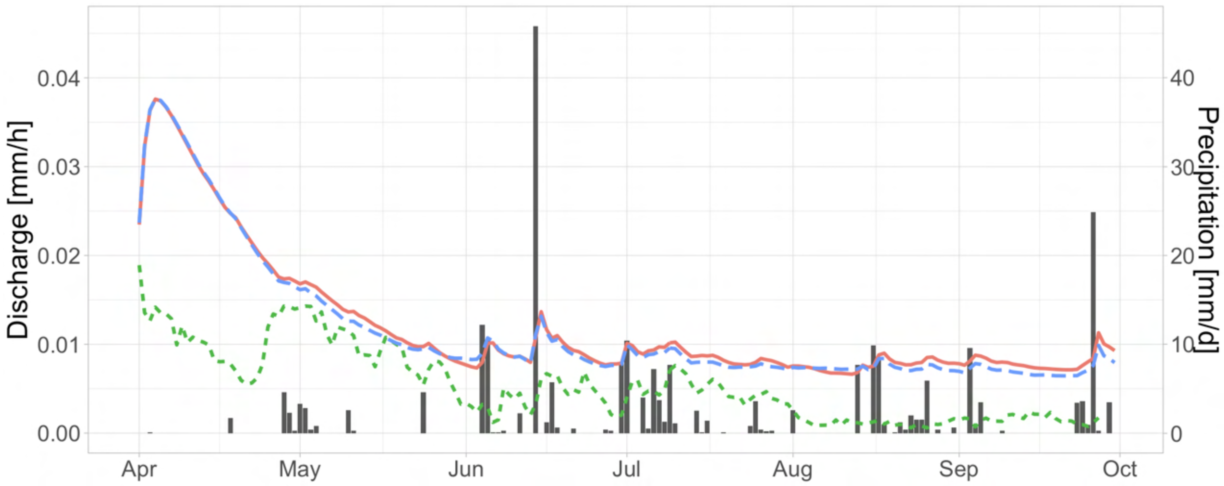

(b) Grote Waterleiding

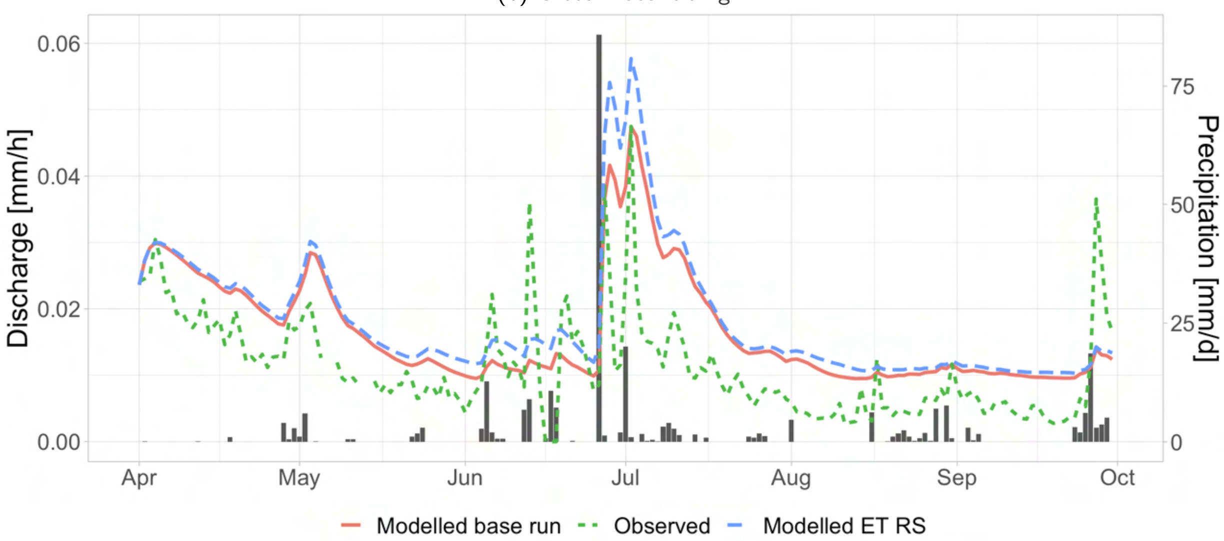

(c) Aa

Figure 4.12: Discharge model simulation (red and blue) and the observed discharge at the catchment outlet. The daily summed precipitation is illustrated with the black columns.

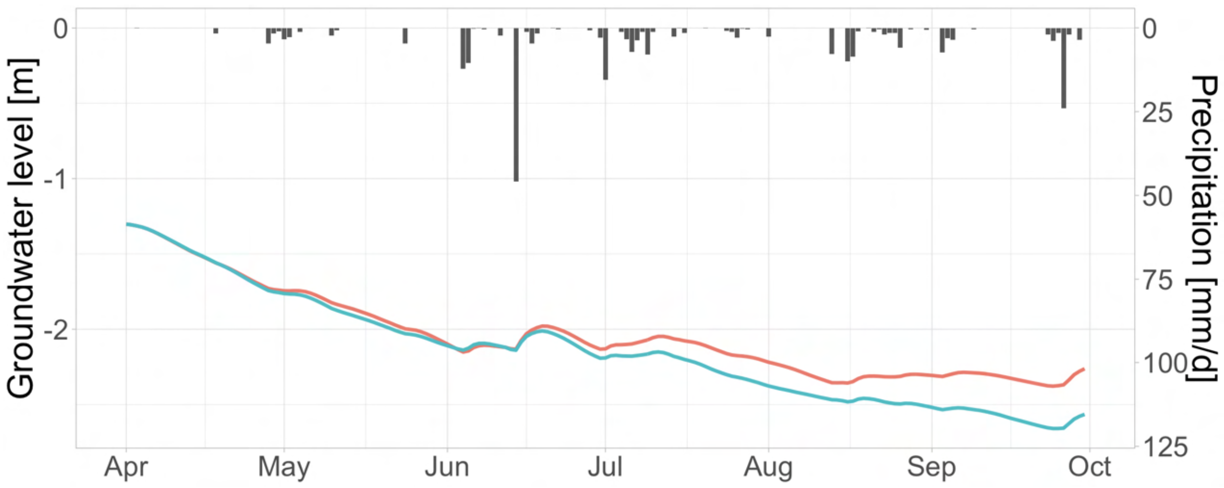

(a) Hupsel

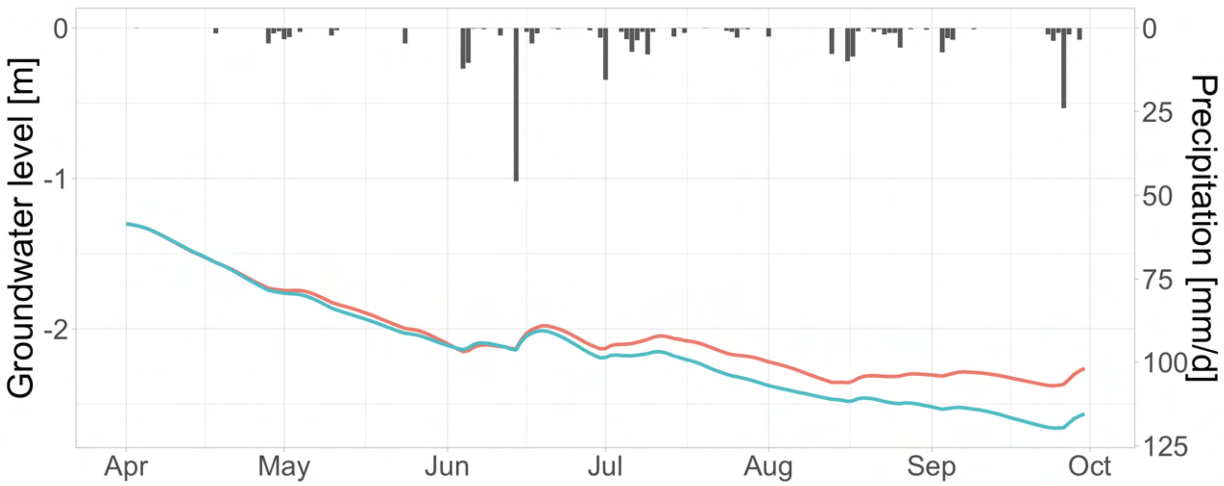

(b) Grote Waterleiding

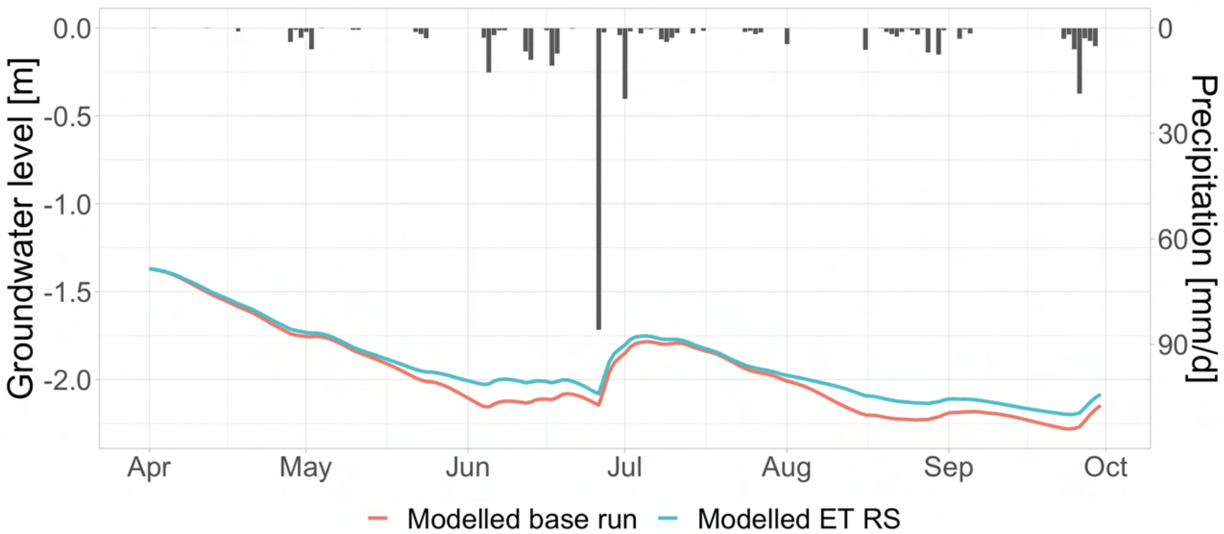

(c) Aa

Figure 4.13: Simulation of the groundwater levels for the three catchments. The daily summed precipitation is illustrated with the black columns.

Table 4.5: The water balance components with the summed values over the growing season of 2020.

		P	ET_{act}	Q	f_{XG}	f_{XS}	d_V	h_Q	h_S
		[mm]	[mm]	[mm]	[mm]	[mm]	[mm]	[mm]	[mm]
Hupsel	Baserun	251	398	6.6	0	0	-153	0	-1
	RS	251	466	5.7	0	0	-219	0	-1
Grote Waterleiding	Baserun	251	426	52.6	0	40	-187	0	-0.4
	RS	251	495	51	0	40	-254	0	-0.5
Aa	Baserun	288	478	73	66	48	-148	0	-0.4
	RS	288	459	80	66	48	-137	0.1	-0.4

Up until July, the simulations are similar, where-after the ET_{RS} simulations starts decreasing.

The water balance demonstrates the amount of water that leaves or enters the catchment. For each catchment, the balance has been made for both the baserun and the ET_{RS} model run (4.5). Obviously, the change in amount available water is negative for all simulations, as the ET is higher compared to the incoming precipitation during spring and summer. In this table, the ET_{act} indicates the simulated ET in WALRUS, which takes the water-stress conditions into account.

5 | Discussion

This section gives a more in depth interpretation and discussion of the results. Furthermore, the results from this study are linked with existing literature, and it discusses the effect of certain choices made during the process. The discussion has the same structure as the results.

5.1 Comparison of ET products

In this study, four ET products were compared: ET_{ref} (estimated by KNMI), ET_{pot} (with crop factor), $ET_{\text{act,sim}}$ (modelled actual ET in WALRUS) and ET_{RS} (remotely sensed ET-product by VanderSat). First, the ET at two KNMI stations (Hupsel and Volkel) was compared. There was a significant difference between the estimated ET_{ref} at two KNMI stations, and the estimated ET_{RS} at the two KNMI stations, see table 4.1. The ET_{ref} was considered to be a rough estimation of evapotranspiration, which did not consider the variability in Land Use Land Cover (LULC) and water availability. This could be the cause of ET_{ref} being 10.5 % less than ET_{RS} at KNMI Hupsel, and 12.4 % at Volkel. Moreover, the modelled $ET_{\text{act,sim}}$ and ET_{RS} were expected to be similar, as in both products, the LULC and water availability were included. The comparison of the 4 catchment-averaged ET products showed that daily ET-values were not similar (figure 4.1). The difference between the daily average $ET_{\text{act,sim}}$ and ET_{RS} was 0.38 mm/day at maximum.

The estimations of ET_{act}, i.e. modelled $ET_{\text{act,sim}}$ in WALRUS and ET_{RS}, would preferably be of the same magnitude. However, results showed that the temporal variation of $ET_{\text{act,sim}}$ and ET_{RS} was different (figure 4.1 and 4.3). Both variables are estimated via an indirect method, which implies that the ET_{act} has not been estimated in-situ, with a specific device such as a lysimeter or the eddy-covariance method. As explained in the introduction and methodology, to obtain the $ET_{\text{act,sim}}$, multiple steps have to be executed (chapter 1 and 2.3). Potentially, the use of crop factors resulted in errors, due to insecurities in the estimation and approximation of the crop factors. Furthermore, the $ET_{\text{act,sim}}$ was modelled in WALRUS, with use of the evaporation reduction factor [Brauer et al., 2014a], which is an approximation of the relation of storage deficit and ET. This approximation of the evaporation reduction factor, as well as the storage deficit is not perfect, and could therefore result in under- or over-estimations of $ET_{\text{act,sim}}$.

In principle, the estimated ET_{ref} is assumed to be of good quality in the Netherlands, as the estimations are performed by the Royal Dutch Meteorological Institute [KNMI, 2020]. Moreover, Martens et al. [2018] compared the GLEAM-HR ET-estimations with the in-situ ET_{ref} from KNMI, which showed a median correlation coefficient of 0.78 across for five measurement sites. In turn, GLEAM-HR is used in the ET_{RS} estimations by VanderSat (see chapter 2.3). Results in this study, however, showed an average correlation between ET_{ref} and ET_{RS} of 0.60. Two critical points require attention considering the KNMI data; 1) The ET_{ref} consistently overestimates land evaporation, as the Makkink equation only considers the atmospheric demand for water over a reference grass, and does not account for any land surface control over the flux. However, in areas with tall vegetation such as deciduous and coniferous forest, underestimations of ET are found [De Bruin and Lablans, 1998]. 2) The ET_{ref} is estimated only at the KNMI measurement stations, of which there are 35 in the Netherlands. 3) ET_{ref} is estimated in-situ, which makes that such observations only represent local processes, and can rarely be extended to large areas to represent the catchment heterogeneity [Kalma et al., 2008]. These critical points result in potential errors in the catchment ET-values, when ET_{ref} is integrated for a heterogeneous area of land.

In contrast, the ET_{RS} estimates the ET for raster cells of 100x100 m based on remote sensing imagery in the GLEAM model. Therefore, the ET_{RS} is more suited to give insight in the spatial variation of ET, and indirectly considers influencing factors such as land use and water availability in the GLEAM model. However, the estimation of ET_{RS} requires a variety of variables, based on remotely sensed observations (see section 2.3.2). Therefore, it is worth noting that the model parameterizations, model assumptions, and forcing data in GLEAM-HR, and consecutively in the SatData 3.0 ET_{RS} products can result in bias [Martens et al., 2018]. Furthermore, the GLEAM model distinguishes 4 land use types for which different modules are used. For agricultural areas, crop factors are determined based on satellite imagery, and therefore deviate from the crop factors used in the Makkink evaporation model [Vandersat]. Urban green patches are small scale and are omitted against other types of land use, such as roads and rooftops, which leads to an underestimation of the amount of vegetation in urban areas. According to Vandersat, the underestimations of the amount of vegetation results in an underestimation of the ET_{RS} in urban areas. Further discussion on LULC effects is given in section 5.3.

Before release of the ET_{RS}-data for open access, a reanalysis calculation is performed using the most reliable and validated data as possible. These datsets consist of the reconstructed and validated precipitation data from the KNMI and corrected images for a number of satellite data sources [Vandersat]. The reanalysis calculation of GLEAM-HR consists of dynamic datasets; 1) combined radar and weather station-measured precipitation produced by the KNMI. 2) An aggregation of satellite-based surface temperature and interpolated KNMI stations data. 3) soil moisture, 4) global radiation, 5) Vegetation Optical Depth (VOD), 6) wind speed, 7) air humidity, and 8) water temperature.

Therefore, the modelling of ET_{RS} includes many parameters that influence ET. This would improve the quality of the estimated ET_{RS}. However, no scientific publication has yet been published on the quality and validation of the ET_{RS} estimations by VanderSat [Vandersat].

5.1.1 Periods of interest

During the analysis on the difference between the ET products, four periods caught special attention as the difference was relatively large between the ET products. The cause of the large variety will now be discussed (section 4.1).

Table 5.1 gives the long-term average monthly T, together with the average monthly T in 2020, and the average T during the periods of interest. Accordingly, a strong correlation was found between periods of higher than average T and low precipitation rates. Therefore, it is likely that P and T conditions have resulted in the differences between the ET products, as water availability is the limiting factor in ET_{act} an ET_{RS}. The difference between the ET products was highest for the ET_{act} and ET_{RS}, compared to the ET_{ref} and ET_{pot}.

Periods with relatively high T and low P-rates, result in decreasing soil moisture content, especially in the top soil. Balugani et al. [2018] described this phenomenon for a semi-arid area. The evaporation of water takes place at the vaporization plane, which is at the beginning of the ET-cycle, at the soil surface. As ET progresses, liquid water flows upward due to capillary flow, driven by the water pressure gradient. As a consequence, the drying front, which marks the transition between saturated and unsaturated zone, increases, and the water table moves down. The vaporization plane moves below the soil surface, and water starts evaporating below the soil surface, and then moves through the dry soil layer. This stage is illustrated in figure 5.1. Vegetation types with a low rooting depths, such as grass, may experience the effects explained by [Balugani et al., 2018]. However, Buitink et al. [2020] showed that for the 2018 summer droughts in the Netherlands, decrease in soil moisture proceeded into deeper layers with time, as root water uptake shifted predominantly to those layers. As the dry periods of 2020 were less extreme compared to the 2018 summer drought, and the studied catchments contain vegetation, the phenomenon explained by Balugani et al. [2018] is assumed to be less relevant.

Table 5.1: Long-term, monthly, and period average temperatures for the Hupsel Brook catchment

	Temperature		
Month	Long-term avg.	2020 avg.	Period avg.
May	12.3	13.1	16.1
June	15.2	17.5	20.3
August	16.7	20.4	22.6
September	14.2	15.2	15.3

During the reanalysis of the ET_{RS}, soil moisture data is used to correct for the phenomenon explained above. Even though the Dutch climate is not classified as a semi-arid, the short periods of dry and hot weather can result in the same phenomenon. The ET_{act} was modelled in WALRUS, and the effect of dry spells is considered in the groundwater-vadose zone (see figure 3.1). Clearly, the ET_{ref} and ET_{pot} estimate high ET-rates due to the high temperature conditions. However, decreasing soil moisture content result in lower ET-rates. The difference between the modelled ET_{act} and ET_{RS} remains a point of discussion, as to which of the two methods represent the 'true' ET at best.

Another explanation of the low ET_{RS} during the dry periods lies in the plant physiology. Changes in stomatal opening are a primary, rapidly occurring effect of drought and heat stress in vegetation [Reynolds-Henne et al., 2010]. Elevated temperatures were shown to result in low air humidity, which negatively affects photosynthesis. Plants therefore, have shown to close their stomata, to prevent excessive loss of water [Schulze et al., 1972].

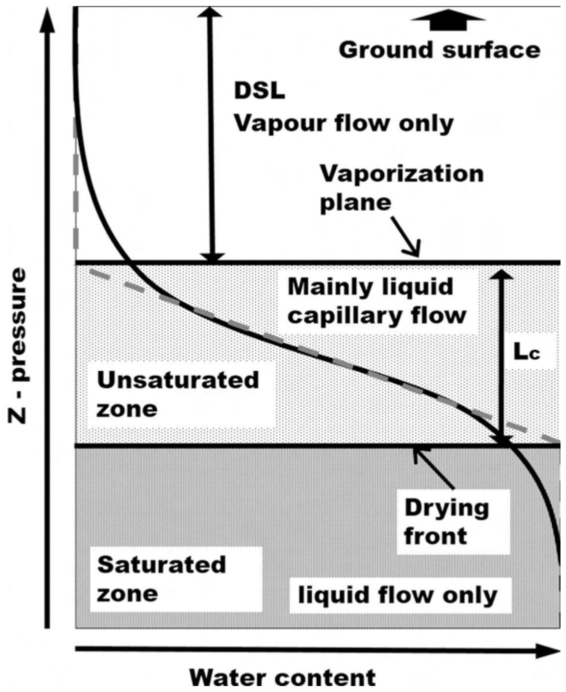

Figure 5.1: Schematics of the soil saturations during stage two evaporation. The dashed grey line is the linearization of the retention curve, the black curve is the water saturation profile of the soil [Balugani et al., 2018]

The stomatal response to the high temperatures during the dry periods of 2020 could therefore be an explanation of the low ET_{RS} rates.

5.2 Spatial and temporal variability of RS ET

The comparison of the ET products was mainly focused on the temporal variety of the estimations. Besides the temporal analysis, the ET_{RS} was used to analyze the spatial variation of ET on a catchment scale. In this section, the spatial variability of ET_{RS} is discussed, and possible weaknesses in the methodology are addressed. In addition, possible environmental factors that influence the spatial pattern of ET_{RS} are mentioned based on existing literature.

5.2.1 Spatial variability of ET in three catchments

For each raster cell with a resolution of 100x100 m, the daily ET_{RS} was estimated. Therefore, the basic statistics that were shown in table 4.3 illustrate the variability of ET in both time (days of growing season) and space (raster cells in catchment). With an average ET_{RS} of 2.70 mm/d, the Grote Waterleiding had the highest evaporation rate during the growing season of 2020. The spatial distribution of the ET_{RS} was mapped in figure 4.5, and shows that the Grote Waterleiding consists for a significant percentage of values in the range of 2.8 - 3.2 mm/d, especially compared to the Hupsel and Aa catchment.

The visual representation of the spatial variation of ET_{RS} in the Hupsel Brook catchment results in the assumption that the ET_{RS} is more homogeneously distributed, compared to the other catchments, with a significant percentage of the average ET_{RS}-values in the range of 2.2-2.9 mm/d. However, the frequency distributions showed that especially the Hupsel Brook and Grote Waterleiding catchment follow roughly the same distribution. The spatial illustration of the standard deviation of ET_{RS} shows that it is heterogeneously distributed. The standard deviation was used to identify the temporal variation of ET_{RS} for each raster cell. In all catchments, areas with low average ET_{RS} also have a low standard deviation of ET_{RS} (figures 4.5 & 4.6).

5.2.2 Linking spatial variability to environmental factors

A quantitative comparison of the average ET_{RS} and standard deviation was illustrated in figure 4.7 and 4.8. The distribution for average ET_{RS} of the Hupsel Brook and Grote Waterleiding catchment was left-skewed, whereas the Aa catchment follows an asymmetrical distribution with two peaks. Miralles et al. [2011] applied the GLEAM-model to analyse the land evaporation distribution on a global scale, and found that roughly 80% of the contribution to ET results from plant transpiration. Therefore, distribution differences between the catchments could be linked to differences in land use between the catchments, as grasslands contribute for 60% to the land use in the Hupsel Brook and Grote Waterleiding catchments (figure 2.3). The effect of land use was analysed in more detail, as it is an essential factor in the calculation of ET_{pot}, with the use of the crop factor. A detailed discussion on the land use effects is given in section 5.3. Other potential environmental factors are soil types, soil texture and geology, elevation and groundwater levels. As the Aa catchment has the largest catchment area, the ET_{RS} could be influenced by a more heterogeneous distribution of the environmental factors. Ultimately, this would imply increased variability of ET_{RS}. In this study, a rough analysis was performed on the correlation between the ET_{RS} and the potential environmental factors. The three catchments have similar soil textures for the top soils, specifically fine and loamy sands (chapter 2). Furthermore, no significant differences in the lowland catchments were found concerning elevation differences and groundwater-depths. Therefore, no evident result was found that explained the difference between the frequency distributions of the three catchments. Even though the low ET_{RS} contributes significantly to the asymmetrical distribution of the Aa catchment, no evidence was found that the environmental factors caused the low ET_{RS}. A more in-depth study on the origin of ET_{RS}'s spatial variability is a valid topic for further research.

5.2.3 Geo-statistical analysis

Experimental variograms were computed for the average and standard deviation of ET_{RS}, for all three catchments. In this study, the experimental variograms were fitted with an exponential semi-variogram model, which resulted in geostatistical elements (table 4.4). The nugget semi-variance expressed as ratio of the total semi-variance (sill), enables comparison of the nugget effect among the different statistical properties and the catchments [Cambardella et al., 1994]. This nugget-to-sill ratio is used to define distinct classes of spatial dependence, as follows: if the ratio was < 0.25, the variable was considered strongly spatially dependent; if the ratio was between 0.25 and 0.75, the variable was considered moderately spatially dependent; and if the ratio was > 0.75, the variable was considered weakly spatially dependent [Cambardella et al., 1994]. All semivariograms indicated strongly spatial dependence, except for the standard deviation of ET_{RS} for the Aa catchment, which was qualified as moderately spatially dependent (table 4.4). The average ET_{RS} for the Aa catchment was considered strongly spatial dependent, however, with ratio of 0.24 it is close to the class of moderately spatial dependence.

Webster and Oliver [2007] stated that sample variances of skewed variables are unstable. This means that if the distribution of the variable is skewed, then the confidence limits on the variogram are wider than they would otherwise be, and as a result the semivariances are less reliable. The frequency distribution of the Hupsel Brook and Grote waterleiding catchment were slightly left-skewed, however, the range of the ET_{RS} is small. For the Aa catchment however, the peak at low ET_{RS} explicitly resulted in a asymmetrical distribution. Therefore, the statement on the spatial dependence for the Aa catchment should be taken with care [Webster and Oliver, 2007].

The range of ET_{RS} implies that the length of the spatial auto-correlation is longer than the size of the raster cells [Chen and Feng, 2013], especially for the Aa catchment. The explanation partly lies within the difference in catchment area, as the range increases with the catchment size.

5.2.4 Period of interest

The periods of interest were of importance, as the ET products differed significantly from each other during these time spans. Therefore, insight in the spatial distribution of the ET_{RS} was of interest. Figure 4.10 and .9 illustrated the spatial distribution of average and standard deviation of ET_{RS} for the Hupsel Brook catchment. Whereas the ET_{RS} ranges from 1.6 to 3.5 averaged over the growing season, the ET_{RS} was lower during period A (figure 4.10), C and D (figure .9). During period B, the ET_{RS} were significantly higher compared to the average of the growing season. As discussed in section 5.1.1, the ET_{RS} responded differently to the P and T conditions during the periods of interest. The phenomenon explained by Balugani et al. [2018] resulted in drops in evaporation, and thus lower ET_{RS}-rates, for period A, C and D. However, period B showed significantly higher ET_{RS}-rates. The Hupsel Brook catchment experienced an precipitation event with $46mm$ rainfall in 24 hours, on the 14th of June. Potentially, before and during dry period B, the water availability was high due to the amount of P in the previous days. This could have resulted in higher soil moisture availability, and increased ET_{RS}-rates. In this study, no analysis was performed on the linkage between soil moisture availability and ET_{RS}. However, this is recommended for further research, as the soil moisture is an important input variable in the GLEAM model [Martens et al., 2017a].

5.3 Land use

In this study, the LGN2020 dataset was used to analyse the effect of land use on the spatial variability of ET_{RS}. The distribution of each of the 13 land use classification was illustrated, combined with a boxplot indicating the mean, and 1st and 3rd quantile (figure 4.11). However, the mean ET_{RS} showed no significant difference between the land use types, even though this was expected due to the use of crop factors in the calculation of ET_{pot} (appendix .1). The mean ET_{RS} for the LULC classes ranged from 2.47 mm/day to 2.65 mm/day.

Vandersat stated that underestimations of ET_{RS} in cities occur due to underestimations of the vegetation patches in urban areas. In addition, lower wind speeds, lower albedo's, and a limited storage capacity in the soil result in lower ET rates [Vandersat]. Therefore, lower ET_{RS} were expected for urban LULC classifications, such as built-up and infrastructure. However, no significant difference of the built-up and infrastructure was found compared to the other LULC classifications.

Already mentioned in 5.1, the GLEAM model considers four land use classifications; high vegetation, low vegetation, bare soil, open water. However, in this study, the effect of ET_{RS} was studied on 13 LULC classifications. As grass can be classified as low and forest as high vegetation, the difference in ET_{RS} is expected between these two LULC classes. However, the mean ET_{RS} was 2.52 mm/day for grass and 2.58 mm/day for forest.

Subsequently, the results were not as expected. There are possible explanations, which will be discussed. The discrete classification of land use in the LGN2020, led to no significant results. The LGN2020 dataset contained 48 different land use classes, which were aggregated to 13 classes in this study. Potentially, combining several land use classification decreased the differences in the land use characteristics. Besides that, GLEAM uses satellite-based maps of LULC that classify per pixel the percentage of forest, short vegetation, bare soil and water. The urban areas are not explicitly modelled in any of the algorithms of GLEAM, but are associated with a large fraction of bare soil and high land surface temperatures. However, visual inspection of the satellite maps showed that urban areas contain reasonable surfaces with vegetation, such as bushes, trees and gardens. Therefore, the effect of urban areas might have been overestimated.

Other studies have showed succesfull results in linking the ET variability to LULC properties such as Normalized Difference Vegetation Index (NDVI) and Leaf Area Index (LAI) which collectively express the percentage of leaf area covering the land to the total area of cultivated land. Nsiah et al. [2021] estimated the spatial distribution of ET within the Pra River basin in Ghana, and also linked the ET to variables NDVI and LAI. Nsiah et al. [2021] specified four land use classes, among which: 1) water, 2) settlement, 3) forest and 4) logged forest. The results showed that uncultivated forest and water bodies record high ET while settlement and bare landscapes record low ET. Similar results were found by Beg et al. [2016] at Tatra mountains in southern Poland and Sun et al. [2011] in Shandong and Jiangsu provinces, China. Therefore, a different methodology would result in better results with linking the ET variability to LULC properties.

Currently, no literature was found with similar results for a humid climate in a lowland catchment as found in Nsiah et al. [2021]. Therefore, further research is desirable, in order to investigate the effect of LULC on ET. If no significant results would come out of that study, further research is required on the use of crop factors for the calculation of ET_{pot}.

5.4 Hydrological model

The performance of the WALRUS hydrological model was examined with the Nash-Sutcliffe efficiency. These values for each model run were given in table 4.6. The model runs during the growing season of 2020, i.e. base run and ET_{RS}-run, showed a maximum NSE of 0.08 for the Hupsel base run. All other NSE-values were below that, and thus classified as unsatisfactory [Yin et al., 2017]. Potential explanations are discussed in this section.

The WALRUS hydrological model is suitable for lowlands where shallow groundwater and surface water influence runoff generation [Brauer et al., 2014a]. The catchment discharge is lowest during the growing season, as a significant percentage of the stored and incoming water leaves the system via evapotranspiration. These low discharges were found for all three catchments (figure 4.12).

Figure 5.2 illustrates the 9 months initialization run for the Aa catchment. The average discharge during the months January, February and March, was 15.9 m^3s^-1 for the observed discharge and 21.7 m^3s^-1 for the modelled base run. The growing season discharge is 6 times lower compared to the discharge during January, February and March.

The 9 months initialization run had a very good performance of the simulated discharge (table 4.6), even though the mean discharge values differ significantly. The relative difference between observed and modelled discharge during the growing season is almost negligible in the 9 months run, which results in a very good model performance. However, the difference in observed and modelled discharge is not negligible for the grow-

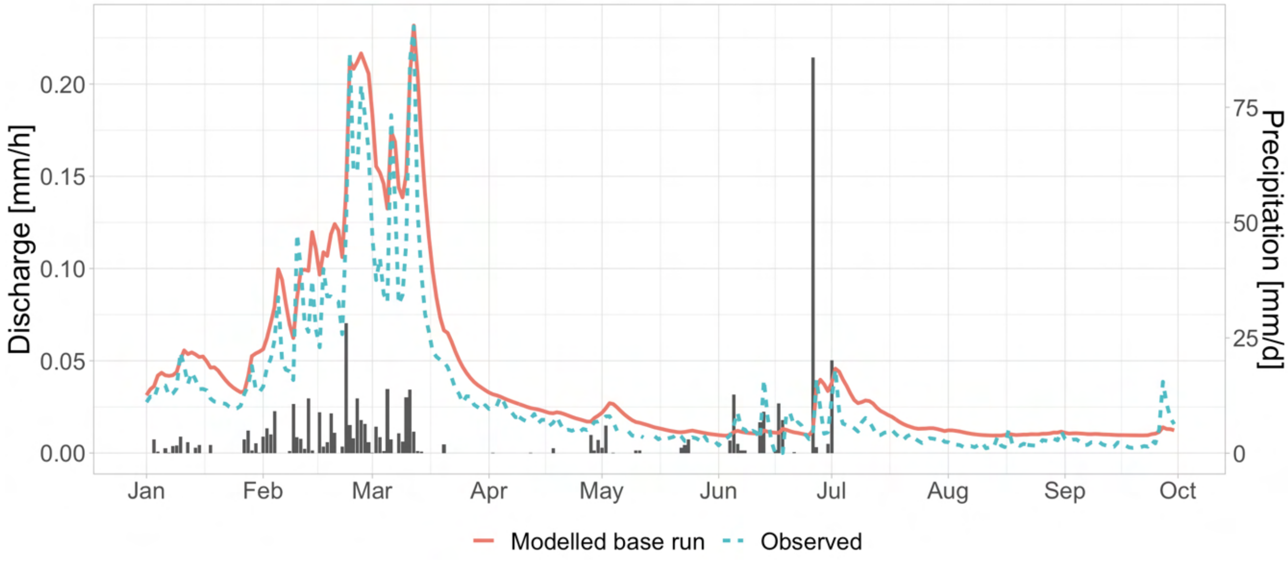

Figure 5.2: Modelled base run and observed discharge for the 9 months initialization run, for the Aa catchment.

ing season model runs, as the discharge range is significantly lower. This results in a unsatisfactory model performance, according to the NSE-values. WALRUS performs well with high discharge peaks during the winter period, however, the model performance lacks in the simulation of a dry growing season. Simulations during wet growing seasons would potentially result in better discharge simulations. However, as the effect of ET on discharge is solely observed during periods of high ET-rates, i.e. spring and summer, differences in model performances due to different ET products would be insignificant.

As the model performances are unsatisfactory for the base run and ET_{RS}-run, statements on whether a certain ET-product results in better model performance are difficult to make. Whereas the NSE-values of the Hupsel Brook and Aa catchment were similar, the NSE-value of the Grote Waterleiding model simulations was lower. The meteorological data used for the Grote Waterleiding was measured at KNMI-weather station the Hupsel, and therefore questionable whether the measured data represents the meteorological conditions in the Grote Waterleiding catchment. The Grote Waterleiding simulated discharge increased in the beginning of April, whereas this was not observed in the measurements of discharge and precipitaiton . Even though the initial conditions (dG_0, dV, hS and hQ) on the 1st of April were used as input, the f_{GS}-flux (groundwater-drainage) is large, and results in increasing discharge in the first half of April.

6 | Conclusion

The aim of this study was to identify the applicability of remotely sensed evapotranspiration (ET_{RS}) in the rainfall-runoff model WALRUS, instead of the indirect point-scale measurements of reference evapotranspiration (ET_{ref}) estimated by KNMI, for three lowland Dutch catchments (Hupsel Brook, Grote Waterleiding, Aa). The ET_{RS}-product computed and reanalysed by VanderSat was used, as the area-covering ET results in insights of spatial variability. Water boards in the east of the Netherlands had shown interest in the use of ET_{RS}, to improve their water management, as the increasing occurrence of droughts during the growing season poses new challenges.

The analysis of the different ET products indicated that significant spatial and temporal differences in measurements occur. Time series of the growing season 2020 showed similar patterns of the four ET products. However, during a period with high temperatures, and lack of precipitation, the ET_{RS} was significantly lower compared to ET_{ref}. Even though WALRUS simulated actual evapotranspiration ($ET_{\text{act,sim}}$) and ET_{RS} both consider LULC and water stress effects, the estimated ET rates were different. Literature showed that high temperatures and lack of precipitation lead to decreased water availability in the top soil, which would eventually lead to significant drops in ET-rates.

Secondly, the ET_{RS} was used to analyze the spatial distribution of ET in the selected catchments. Areas with low temporal average ET_{RS} also have a low standard deviation. The spatial analysis showed a range of 1.5 mm/day in temporal averaged ET_{RS} values. The spatial variability was not correlated with such as soil types, soil texture and geology, elevation and groundwater levels. Furthermore, this study found no evidence that the land use significantly influences the spatial variability of ET_{RS}.

Finally, it has been proven that ET as input in the rainfall-runoff model WALRUS, has no significant influence on the discharge simulations. This was found for the growing season 2020, which was drier than average. During the growing season, the loss of water due to evapotranspiration, combined with lack of precipitation, strongly reduced the availability of water. As a result, less water left the system via discharge. For the lowland catchments, in a humid climate, the use of an ET-product with catchment averaged values in WALRUS is not required in order to obtain better discharge simulations.

Future research should focus on the origin of the differences between the ET products, and which one represents the 'true' ET in a better way. Furthermore, the factor(s) that result in the spatial variability remain unknown, as no explanation was found for the spatial variability in the studied catchments. Therefore, a detailed analysis is required to investigate the correlation with certain environmental factors. While this study showed no significant effect of land use on the ET, other factors such as the NDVI and LAI could lead to more significant results.

Acknowledgements

First off, I would like to thank my supervisors Claudia and Martine. For their time, the helpful discussions and tips, feedback on parts of my report and the additional insights in processing data and results. Secondly, I would like to thank Jos Moorman from Wa- terschap Aa en Maas, who provided the discharge data of the Aa. I would also thank the other data providers; KNMI for the meteorological data, VanderSat for the remotely sensed evapotranspiration product, and Waterboard Aa en Maas and Waterboard Rijn en IJssel for the discharge data. Furthermore, I would like to thank all the other thesis students who have provided me with useful feedback during the thesis rings. Lastly, I want to thank my girlfriend, family and friends for their support and interest in my thesis project. Thanks for the support, and listening to me whenever I wanted to talk about the thesis project.

Bibliography

R. G. Allen, L. S. Pereira, D. Raes, M. Smith, et al. Crop evapotranspiration-guidelines for computing crop water requirements-fao irrigation and drainage paper 56. *Fao, Rome*, 300(9):D05109, 1998.

C. Alvarez-Garreton, D. Ryu, A. Western, W. Crow, and D. Robertson. The impacts of assimilating satellite soil moisture into a rainfall–runoff model in a semi-arid catchment. *Journal of hydrology*, 519:2763–2774, 2014.

R. N. Armstrong, J. W. Pomeroy, and L. W. Martz. Spatial variability of mean daily estimates of actual evaporation from remotely sensed imagery and surface reference data. *Hydrology and Earth System Sciences*, 23(12):4891–4907, 2019.

E. Balugani, M. Lubczynski, C. Van Der Tol, and K. Metselaar. Testing three approaches to estimate soil evaporation through a dry soil layer in a semi-arid area. *Journal of hydrology*, 567:405–419, 2018.

W. Bastiaanssen, E. Noordman, H. Pelgrum, G. Davids, B. Thoreson, and R. Allen. Sebal model with remotely sensed data to improve water-resources management under actual field conditions. *Journal of irrigation and drainage engineering*, 131(1):85–93, 2005.

W. G. Bastiaanssen, M. Menenti, R. Feddes, and A. Holtslag. A remote sensing surface energy balance algorithm for land (sebal). 1. formulation. *Journal of hydrology*, 212:198–212, 1998.

A. A. F. Beg, A. H. Al-Sulttani, A. Ochtyra, A. Jarocińska, and A. Marcinkowska. Estimation of evapotranspiration using sebal algorithm and landsat-8 data—a case study: Tatra mountains region. *Journal of Geological Resource and Engineering*, 6:257–270, 2016.

C. Brauer, A. Teuling, P. Torfs, and R. Uijlenhoet. The wageningen lowland runoff simulator (walrus): a lumped rainfall–runoff model for catchments with shallow groundwater. *Geoscientific model development*, 7(5):2313–2332, 2014a.

C. Brauer, P. Torfs, A. Teuling, and R. Uijlenhoet. The wageningen lowland runoff simulator (walrus): application to the hupsel brook catchment and the cabauw polder. *Hydrology and Earth System Sciences*, 18(10): 4007–4028, 2014b.

C. Brauer, Y. van der Velde, A. Teuling, and R. Uijlenhoet. The hupsel brook catchment: Insights from five decades of lowland observations. *Vadose Zone Journal*, 17(1):1–8, 2018.

J. Buitink, A. M. Swank, M. van der Ploeg, N. E. Smith, H.-J. F. Benninga, F. van der Bolt, C. D. Carranza, G. Koren, R. van der Velde, and A. J. Teuling. Anatomy of the 2018 agricultural drought in the netherlands using in situ soil moisture and satellite vegetation indices. *Hydrology and earth system sciences*, 24(12):6021–6031, 2020.

C. A. Cambardella, T. B. Moorman, T. Parkin, D. Karlen, J. Novak, R. Turco, and A. Konopka. Field-scale variability of soil properties in central iowa soils. 1994.

L. Chen and Q. Feng. Geostatistical analysis of temporal and spatial variations in groundwater levels and quality in the minqin oasis, northwest china. *Environmental earth sciences*, 70(3):1367–1378, 2013.

A. Clulow, C. Everson, M. Mengistu, J. Price, A. Nickless, and G. Jewitt. Extending periodic eddy covariance latent heat fluxes through tree sap-flow measurements to estimate long-term total evaporation in a peat swamp forest. *Hydrology and Earth System Sciences*, 19(5):2513–2534, 2015.

R. D. Cook. Detection of influential observation in linear regression. *Technometrics*, 19(1):15–18, 1977.

H. De Bruin and W. Lablans. Reference crop evapotranspiration determined with a modified makkink equation. *Hydrological Processes*, 12(7):1053–1062, 1998.

J. Gash. An analytical model of rainfall interception by forests. *Quarterly Journal of the Royal Meteorological Society*, 105(443):43–55, 1979.

T. Gerritsen. Hydrological intercomparison of rain gauge, weather radar and satellite observations, 2019.

E. Gringarten and C. V. Deutsch. Teacher's aide variogram interpretation and modeling. *Mathematical Geology*, 33(4):507–534, 2001.

V. Hari, O. Rakovec, Y. Markonis, M. Hanel, and R. Kumar. Increased future occurrences of the exceptional 2018–2019 central european drought under global warming. *Scientific reports*, 10(1):1–10, 2020.

D. Heuvelink, M. Berenguer, C. C. Brauer, and R. Uijlenhoet. Hydrological application of radar rainfall nowcasting in the netherlands. *Environment international*, 136:105431, 2020.

P. Hiemstra and R. Sluiter. Interpolation of makkink evaporation in the netherlands. -, 2011.

C. Justice, J. Townshend, E. Vermote, E. Masuoka, R. Wolfe, N. Saleous, D. Roy, and J. Morisette. An overview of modis land data processing and product status. *Remote sensing of Environment*, 83(1-2):3–15, 2002.

J. D. Kalma, T. R. McVicar, and M. F. McCabe. Estimating land surface evaporation: A review of methods using remotely sensed surface temperature data. *Surveys in Geophysics*, 29(4):421–469, 2008.

A. Klein Tank, J. Beersma, J. Bessembinder, B. Van den Hurk, and G. Lenderink. Knmi 14: Klimaatscenario's voor nederland. *KNMI publicatie*, 2014.

KNMI. KNMI - Juni 2020, 2020. URL `https://www.knmi.nl/nederland-nu/klimatologie/maand-en-seizoensoverzichten/2020/juni`.

KNMI. Welcome - KNMI Data Platform - KNMI Data Platform, 2021. URL `https://dataplatform.knmi.nl`.

J. Komma, G. Blöschl, and C. Reszler. Soil moisture updating by ensemble kalman filtering in real-time flood forecasting. *Journal of Hydrology*, 357(3-4):228–242, 2008.

F. Li, R. Cao, Y. Zhao, D. Mu, C. Fu, and F. Ping. Remote sensing penman–monteith model to estimate catchment evapotranspiration considering the vegetation diversity. *Theoretical and Applied Climatology*, 127(1-2):111–121, 2017.

G. Makkink and H. Van Heemst. The actual evapotranspiration as a function of the potential evapotranspiration and the soil moisture tension. *Netherlands Journal of Agricultural Science*, 4(1):67–72, 1956.

B. Martens, D. Miralles, L. Hans, R. van der Schalie, R. de Jeu, D. Fernández-Prieto, H. Beck, W. Dorigo, and N. Verhoest. Gleam v3: Satellite-based land evaporation and root-zone soil moisture. *Geoscientific Model Development*, 10, 05 2017a. doi: 10.5194/gmd-10-1903-2017.

B. Martens, D. G. Miralles, H. Lievens, R. Van Der Schalie, R. A. De Jeu, D. Fernández-Prieto, H. E. Beck, W. A. Dorigo, and N. E. Verhoest. Gleam v3: Satellite-based land evaporation and root-zone soil moisture. *Geoscientific Model Development*, 10 (5):1903–1925, 2017b.

B. Martens, R. A. De Jeu, N. E. Verhoest, H. Schuurmans, J. Kleijer, and D. G. Miralles. Towards estimating land evaporation at field scales using gleam. *Remote Sensing*, 10(11):1720, 2018.

Meteobase. Het online archief van historische neerslag en verdamping in Nederland. URL `https://www.meteobase.nl`.

D. Miralles, R. De Jeu, J. Gash, T. Holmes, and A. Dolman. Magnitude and variability of land evaporation and its components at the global scale. *Hydrology and Earth System Sciences*, 15(3):967–981, 2011.

A. F. Moene and J. C. Van Dam. *Transport in the atmosphere-vegetation-soil continuum*. Cambridge University Press, 2014.

Y. Mohamed, W. Bastiaanssen, and H. Savenije. Spatial variability of evaporation and moisture storage in the swamps of the upper nile studied by remote sensing techniques. *Journal of hydrology*, 289(1-4):145–164, 2004.

J. E. Nash and J. V. Sutcliffe. River flow forecasting through conceptual models part i—a discussion of principles. *Journal of hydrology*, 10(3):282–290, 1970.

H. Nouri, S. Beecham, F. Kazemi, A. Hassanli, and S. Anderson. Remote sensing techniques for predicting evapotranspiration from mixed vegetated surfaces. *Hydrology and Earth System Sciences Discussions*, 10 (3):3897–3925, 2013.

J. Nsiah, C. Gyamfi, G. Anornu, and S. Odai. Estimating the spatial distribution of evapotranspiration within the pra river basin of ghana. *Heliyon*, 7(4):e06828, 2021.

G. Papadavid, D. G. Hadjimitsis, L. Toulios, and S. Michaelides. A modified sebal modeling approach for estimating crop evapotranspiration in semi-arid conditions. *Water resources management*, 27(9): 3493–3506, 2013.

M. Pezij, H. Benninga, C. Carranza, D. C. Augustijn, R. van der Velde, and M. van der Ploeg. Bodemvocht uit satellietdata voor optimalisatie waterbeheer. *Land+ water*, 56(7/8):26–27, 2016.

S. Y. Philip, S. F. Kew, K. van der Wiel, N. Wanders, and G. J. van Oldenborgh. Regional differentiation in climate change induced drought trends in the netherlands. *Environmental Research Letters*, 15(9):094081, 2020.

C. H. B. Priestley and R. J. TAYLOR. On the assessment of surface heat flux and evaporation using large-scale parameters. *Monthly weather review*, 100(2):81–92, 1972.

C. E. Reynolds-Henne, A. Langenegger, J. Mani, N. Schenk, A. Zumsteg, and U. Feller. Interactions between temperature, drought and stomatal opening in legumes. *Environmental and Experimental Botany*, 68(1):37–43, 2010.

K. Schneider. Assimilating remote sensing data into a land-surface process model. *International Journal of Remote Sensing*, 24(14):2959–2980, 2003.

E.-D. Schulze, O. Lange, U. Buschbom, L. Kappen, and M. Evenari. Stomatal responses to changes in humidity in plants growing in the desert. *Planta*, 108(3): 259–270, 1972.

Z. Sun, B. Wei, W. Su, W. Shen, C. Wang, D. You, and Z. Liu. Evapotranspiration estimation based on the sebal model in the nansi lake wetland of china. *Mathematical and Computer Modelling*, 54(3-4):1086–1092, 2011.

A. J. Teuling, A. F. Van Loon, S. I. Seneviratne, I. Lehner, M. Aubinet, B. Heinesch, C. Bernhofer, T. Grünwald, H. Prasse, and U. Spank. Evapotranspiration amplifies european summer drought. *Geophysical Research Letters*, 40(10):2071–2075, 2013. doi: https://doi.org/10.1002/grl.50495.

Vandersat. VanderSat SATDATA-3.0 Documentatie — VanderSat 3.0-Champaign documentation. URL https://docs.vandersat.com/satdata/index.html\#introductie.

R. Versteeg, D. Klopstra, E. v.d. Braak, and H. Vreugdehil. Distributiemodel, deel D. Technical report, 2009. URL http://nhi.nu/nl/files/8114/2651/5650/Distributiemodel_deel_D_Zuid_Nederland_2009.pdf.

P. Wagle and P. Gowda. Remote sensing of evapotranspiration (et). *Remote Sensing*, 2019.

Waterschap Rijn en IJssel. Waterdata - waterschap rijn en ijssel - kimare, 2021. URL https://waterdata.wrij.nl/index.php?wat=inleiding.

R. Webster and M. A. Oliver. *Geostatistics for environmental scientists*. John Wiley & Sons, 2007.

WRIJ. Factsheet waterkwaliteit grote waterleiding.

WRIJ. Afvoerkarakteristieken. URL https://www.wrij.nl/statisch/berkel/kopie-2/artikel/.

J. Yin, F. He, Y. J. Xiong, and G. Y. Qiu. Effects of land use/land cover and climate changes on surface runoff in a semi-humid and semi-arid transition zone in northwest china. *Hydrology and Earth System Sciences*, 21(1):183–196, 2017.

Y. Zhang, F. H. Chiew, L. Zhang, and H. Li. Use of remotely sensed actual evapotranspiration to improve rainfall–runoff modeling in southeast australia. *Journal of Hydrometeorology*, 10(4):969–980, 2009.

Appendix

Figure .1: Overview of variables, parameters and functions as given in [Brauer et al., 2014a]. All fluxes are catchment averages, both external ones (including Q and f_{XS}) and internal fluxes (which are multiplied with the relative surface area of the reservoir in question). Note that d_{V}, h_{Q} and h_{S} result from the mass balances in the three reservoirs, while dG is only used as pressure head to compute the groundwater drainage flux. The names of the fluxes are derived from the reservoirs (for example f_{XS}: f stands for flow, the X for external and the S for surface water – water flowing from outside the catchment into the surface water network)

	States		
d_{V}	storage deficit	$\rightarrow \frac{\mathrm{d}d_{\mathrm{V}}}{\mathrm{d}t} = -\frac{f_{\mathrm{XG}}+P_{\mathrm{V}}-\mathrm{ET}_{\mathrm{V}}-f_{\mathrm{GS}}}{a_{\mathrm{G}}}$	(mm)
d_{G}	groundwater depth	$\rightarrow \frac{\mathrm{d}d_{\mathrm{G}}}{\mathrm{d}t} = \frac{d_{\mathrm{V}}-d_{\mathrm{V,eq}}}{c_{\mathrm{V}}}$	(mm)
h_{Q}	level quickflow reservoir	$\rightarrow \frac{\mathrm{d}h_{\mathrm{Q}}}{\mathrm{d}t} = \frac{P_{\mathrm{Q}}-f_{\mathrm{QS}}}{a_{\mathrm{G}}}$	(mm)
h_{S}	surface water level	$\rightarrow \frac{\mathrm{d}h_{\mathrm{S}}}{\mathrm{d}t} = \frac{f_{\mathrm{XS}}+P_{\mathrm{S}}-\mathrm{ET}_{\mathrm{S}}+f_{\mathrm{GS}}+f_{\mathrm{QS}}-Q}{a_{\mathrm{S}}}$	(mm)
	Dependent variables		
W	wetness index	$=\mathrm{func}(d_{\mathrm{V}})$	(–)
β	evapotranspiration reduction factor	$=\mathrm{func}(d_{\mathrm{V}})$	(–)
$d_{\mathrm{V,eq}}$	equilibrium storage deficit	$=\mathrm{func}(d_{\mathrm{G}})$	(mm)
	External fluxes: input		
P	precipitation		$(\mathrm{mm\,h^{-1}})$
$\mathrm{ET}_{\mathrm{pot}}$	potential evapotranspiration		$(\mathrm{mm\,h^{-1}})$
Q_{obs}	discharge (for calibration and Q_0)		$(\mathrm{mm\,h^{-1}})$
f_{XG}	seepage (up/down)/extraction		$(\mathrm{mm\,h^{-1}})$
f_{XS}	surface water supply/extraction		$(\mathrm{mm\,h^{-1}})$
	External fluxes: output		
$\mathrm{ET}_{\mathrm{act}}$	actual evapotranspiration	$=\mathrm{ET}_{\mathrm{V}}+\mathrm{ET}_{\mathrm{S}}$	$(\mathrm{mm\,h^{-1}})$
Q	discharge	$=\mathrm{func}(h_{\mathrm{S}})$	$(\mathrm{mm\,h^{-1}})$
	Internal fluxes		
P_{S}	precipitation into surface water reservoir	$=P\cdot a_{\mathrm{S}}$	$(\mathrm{mm\,h^{-1}})$
P_{V}	precipitation into vadose zone	$=P\cdot(1-W)\cdot a_{\mathrm{G}}$	$(\mathrm{mm\,h^{-1}})$
P_{Q}	precipitation into quickflow reservoir	$=P\cdot W\cdot a_{\mathrm{G}}$	$(\mathrm{mm\,h^{-1}})$
ET_{V}	actual evapotranspiration vadose zone	$=\mathrm{ET}_{\mathrm{pot}}\cdot\beta\cdot a_{\mathrm{G}}$	$(\mathrm{mm\,h^{-1}})$
ET_{S}	actual evapotranspiration surface water	$=\mathrm{ET}_{\mathrm{pot}}\cdot a_{\mathrm{S}}$	$(\mathrm{mm\,h^{-1}})$
f_{GS}	groundwater drainage/surface water infiltration	$=\frac{(c_{\mathrm{D}}-d_{\mathrm{G}}-h_{\mathrm{S}})\cdot\max((c_{\mathrm{D}}-d_{\mathrm{G}}),h_{\mathrm{S}})}{c_{\mathrm{G}}}\cdot a_{\mathrm{G}}$	$(\mathrm{mm\,h^{-1}})$
f_{QS}	quickflow	$=\frac{h_{\mathrm{Q}}}{c_{\mathrm{Q}}}\cdot a_{\mathrm{G}}$	$(\mathrm{mm\,h^{-1}})$
	Model parameters		
c_{W}	wetness index parameter		(mm)
c_{V}	vadose zone relaxation time		(h)
c_{G}	groundwater reservoir constant		(mm h)
c_{Q}	quickflow reservoir constant		(h)
	Supplied parameters		
a_{S}	surface water area fraction		(–)
a_{G}	groundwater reservoir area fraction	$=1-a_{\mathrm{S}}$	(–)
c_{D}	channel depth		(mm)
	User-defined functions with defaults		
$W(d_{\mathrm{V}})$	wetness index	$=\cos\left(\frac{\max(\min(d_{\mathrm{V}},c_{\mathrm{W}}),0)\cdot\pi}{c_{\mathrm{W}}}\right)\cdot\frac{1}{2}+\frac{1}{2}$	(–)
$\beta(d_{\mathrm{V}})$	evapotranspiration reduction factor	$=\frac{1-\exp[\zeta_1(d_{\mathrm{V}}-\zeta_2)]}{1+\exp[\zeta_1(d_{\mathrm{V}}-\zeta_2)]}\cdot\frac{1}{2}+\frac{1}{2}$	(–)
$d_{\mathrm{V,eq}}(d_{\mathrm{G}})$	equilibrium storage deficit	$=\theta_s\left(d_{\mathrm{G}}-\frac{d_{\mathrm{G}}^{1-1/b}}{(1-\frac{1}{b})\psi_{\mathrm{ae}}^{-1/b}}-\frac{\psi_{\mathrm{ae}}}{1-b}\right)$	(mm)
$Q(h_{\mathrm{S}})$	stage–discharge relation	$=c_{\mathrm{S}}\left(\frac{h_{\mathrm{S}}-h_{\mathrm{S,min}}}{c_{\mathrm{D}}-h_{\mathrm{S,min}}}\right)^{x_{\mathrm{S}}}$	$(\mathrm{mm\,h^{-1}})$
	Parameters for default functions		
ζ_1	curvature ET reduction function		(–)
ζ_2	translation ET reduction function		(mm)
b	pore size distribution parameter		(–)
ψ_{ae}	air entry pressure		(mm)
θ_s	soil moisture content at saturation		(–)
c_{S}	surface water parameter: bankfull Q		$(\mathrm{mm\,h^{-1}})$
x_{S}	stage–discharge relation exponent		(–)
$h_{\mathrm{S,min}}$	surface water level when $Q=0$		(mm)

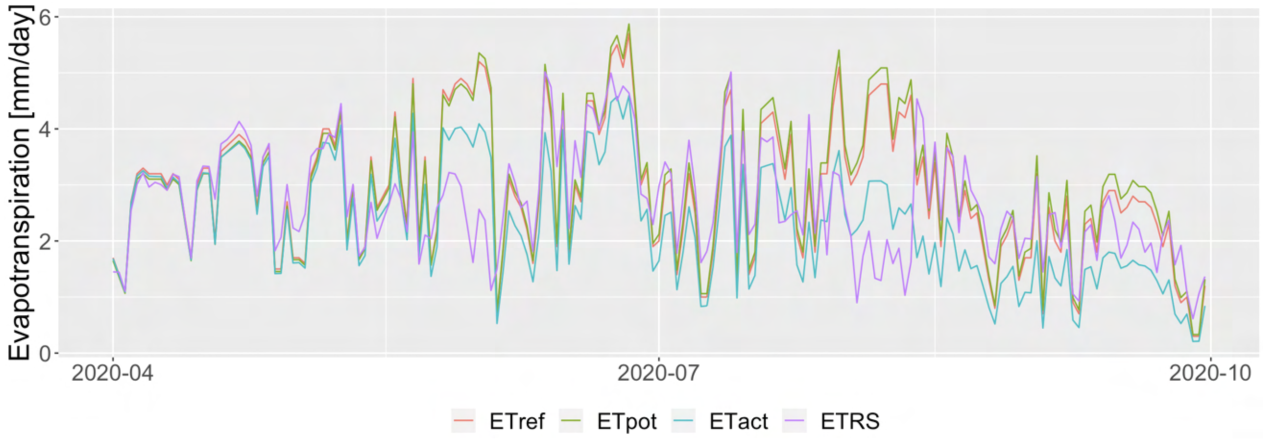

Figure .2: Time series of different ET products during the growing season of 2020, for the Grote Waterleiding catchment

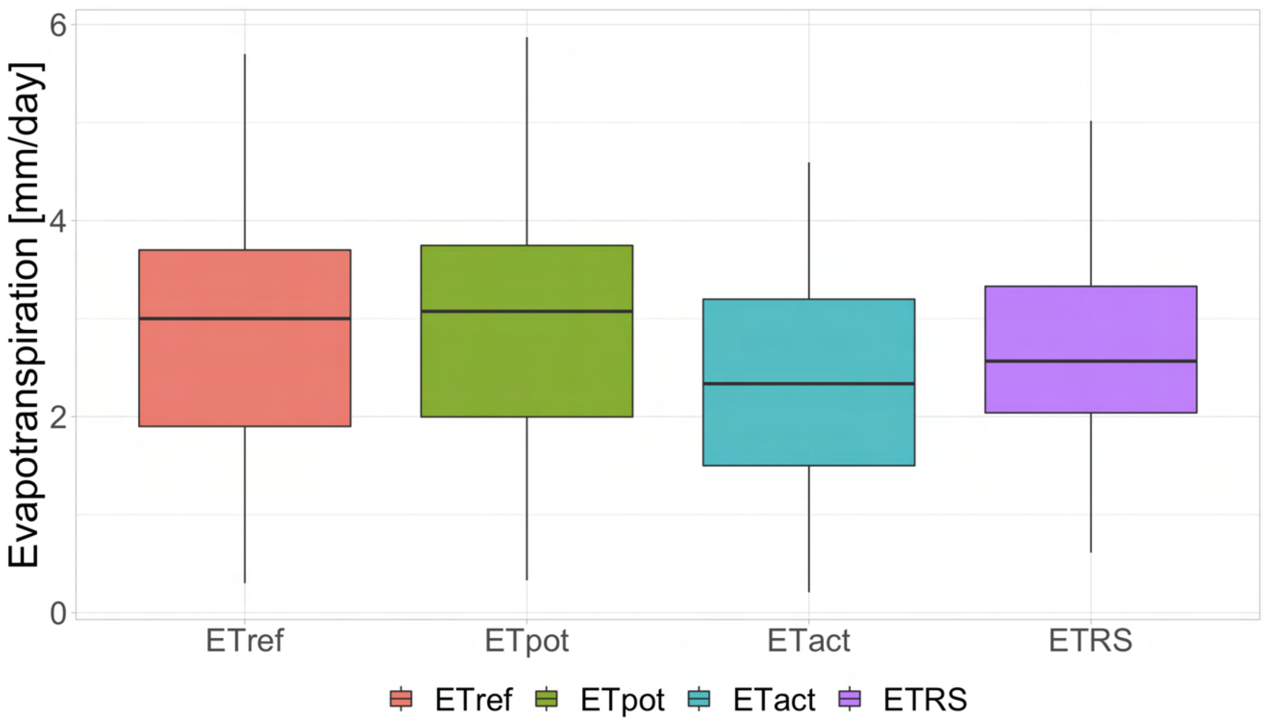

Figure .3: Time series of different ET products during the growing season of 2020, for the Grote Waterleiding catchment

Table .1: Crop factors (K_c) for the defined LULC classifications [Moene and Van Dam, 2014]. The star (*) defines the land use types of which the crop factor was roughly estimated. Occurrence of these land use types was low, thus limited impact was expected

Month	Grass	Maize	Potato	Beet	Grains	Forest	Water	Built up*	Bush vegetation*	Infrastructure*	Heather*	Peat*	Other*	Bare soil
April	1.1	0.5	0.5	0.5	0.8	0.9	1.3	1.0	1.0	1.0	1.1	1.2	1.0	0.5
May	1.1	0.7	0.7	0.5	1.0	0.8	1.3	1.0	1.0	1.0	1.0	1.3	1.0	0.5
June	1.1	1.0	1.1	0.9	1.2	0.9	1.3	1.0	1.0	1.0	1.0	0.9	1.0	0.5
July	1.1	1.3	1.1	1.1	0.9	0.9	1.3	1.0	1.0	1.0	1.0	0.9	1.0	0.5
August	1.1	1.2	1.1	1.2	0.5	0.9	1.2	1.0	1.0	1.0	1.1	0.8	1.0	0.5
September	1.1	1.2	0.7	1.1	0.5	1.1	1.2	1.0	1.1	1.0	1.1	0.8	1.0	0.5

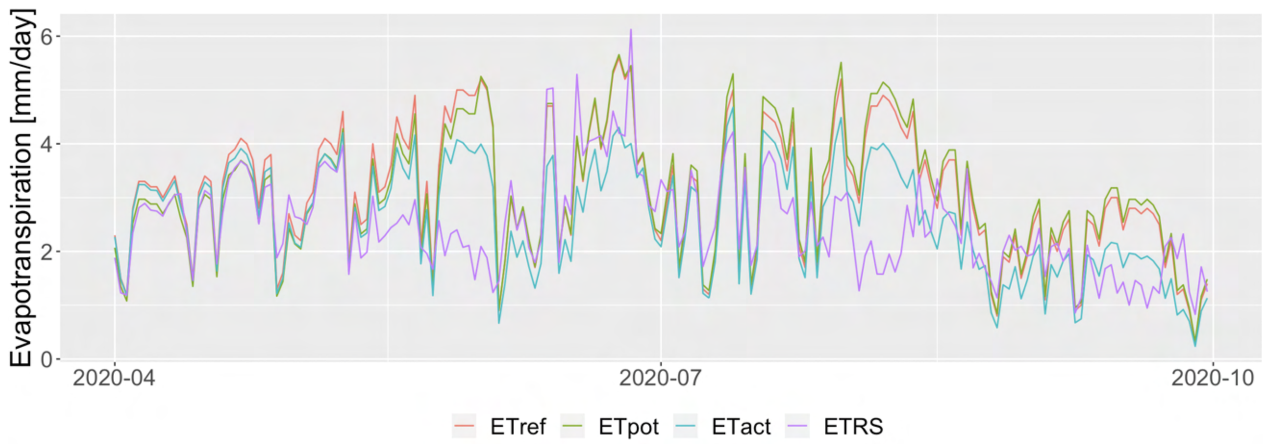

Figure .4: Time series of different ET products during the growing season of 2020, for the Aa catchment

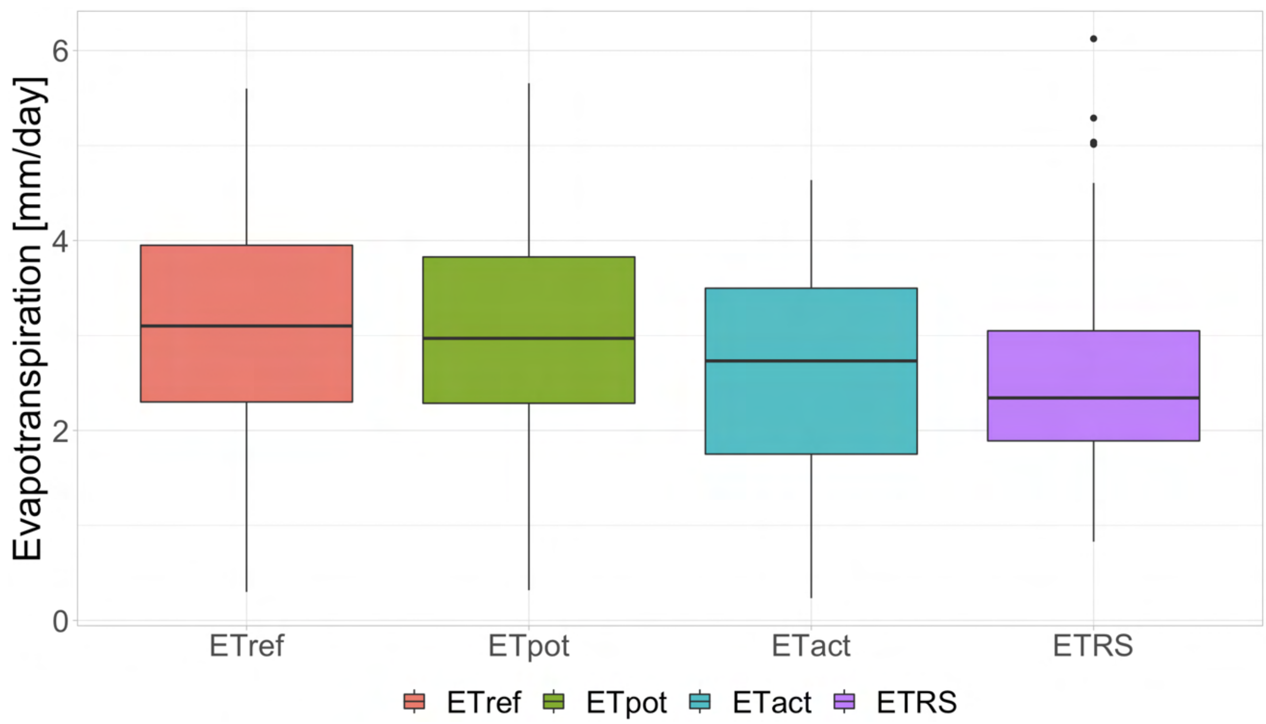

Figure .5: Time series of different ET products during the growing season of 2020, for the Aa catchment

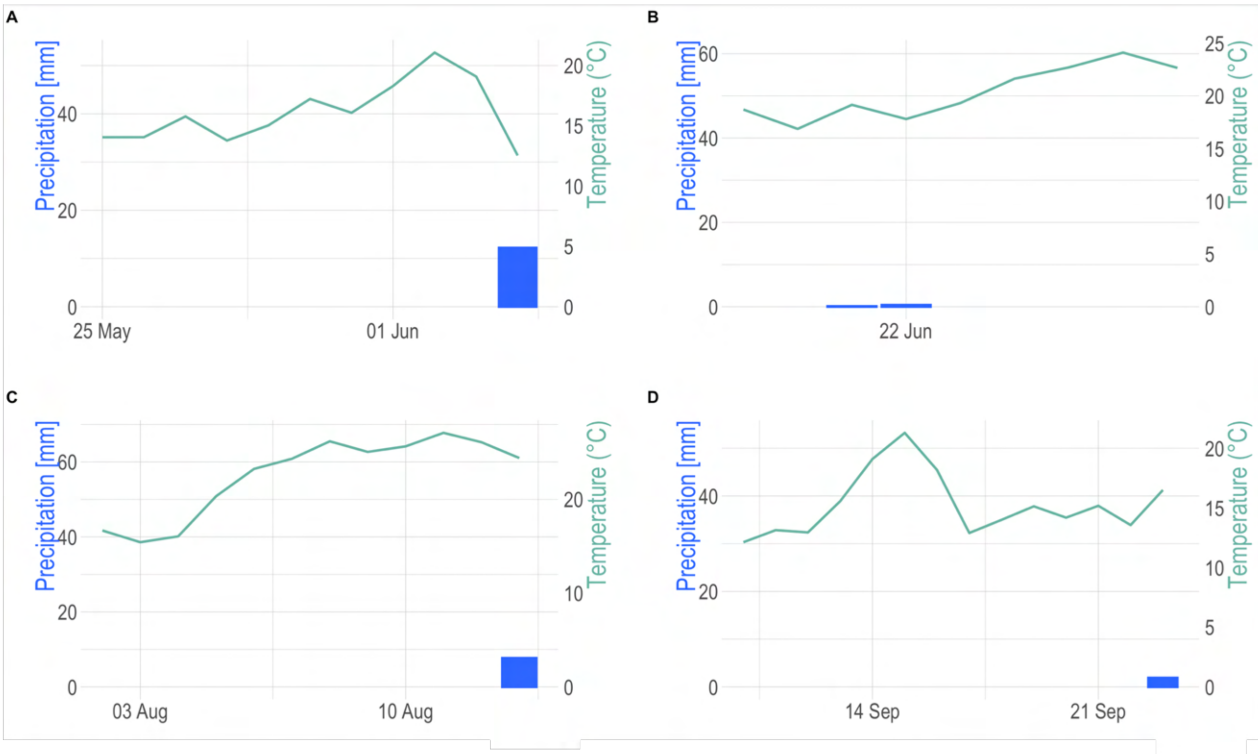

Figure .6: Precipitation events and daily average temperatures during four periods of 2020.

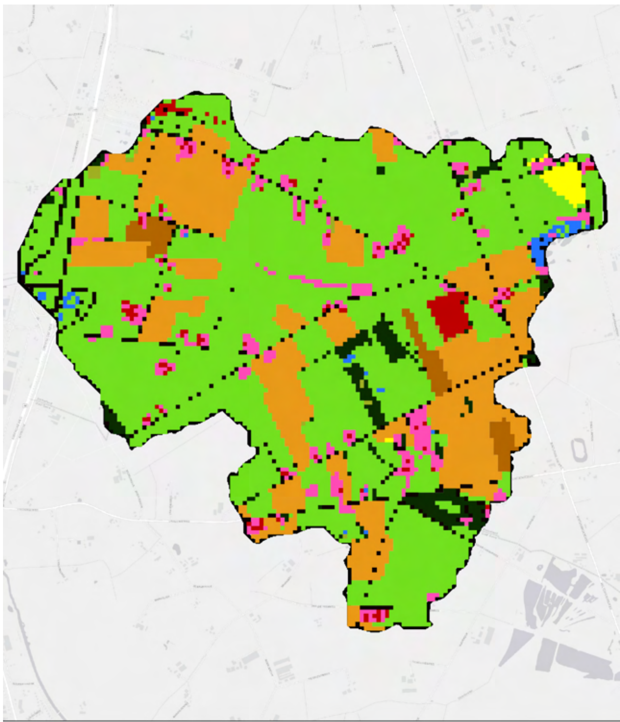

(a) Hupsel Brook catchment

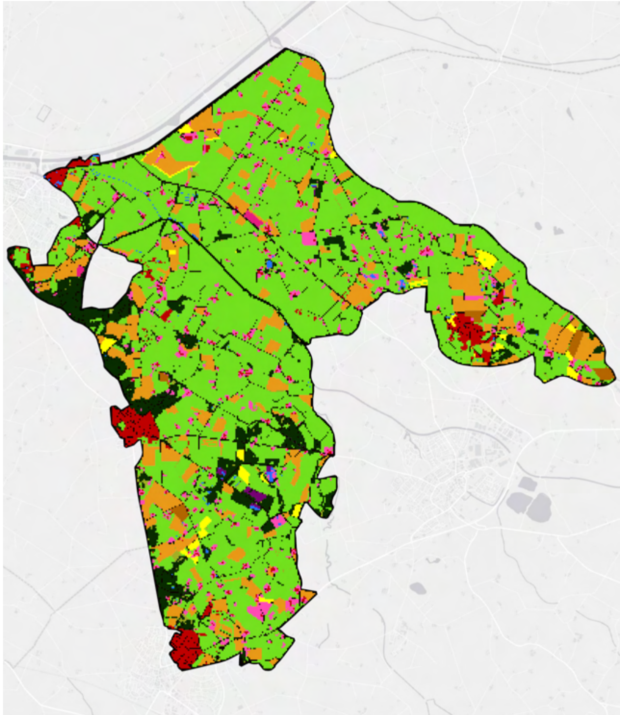

(b) Grote Waterleiding catchment

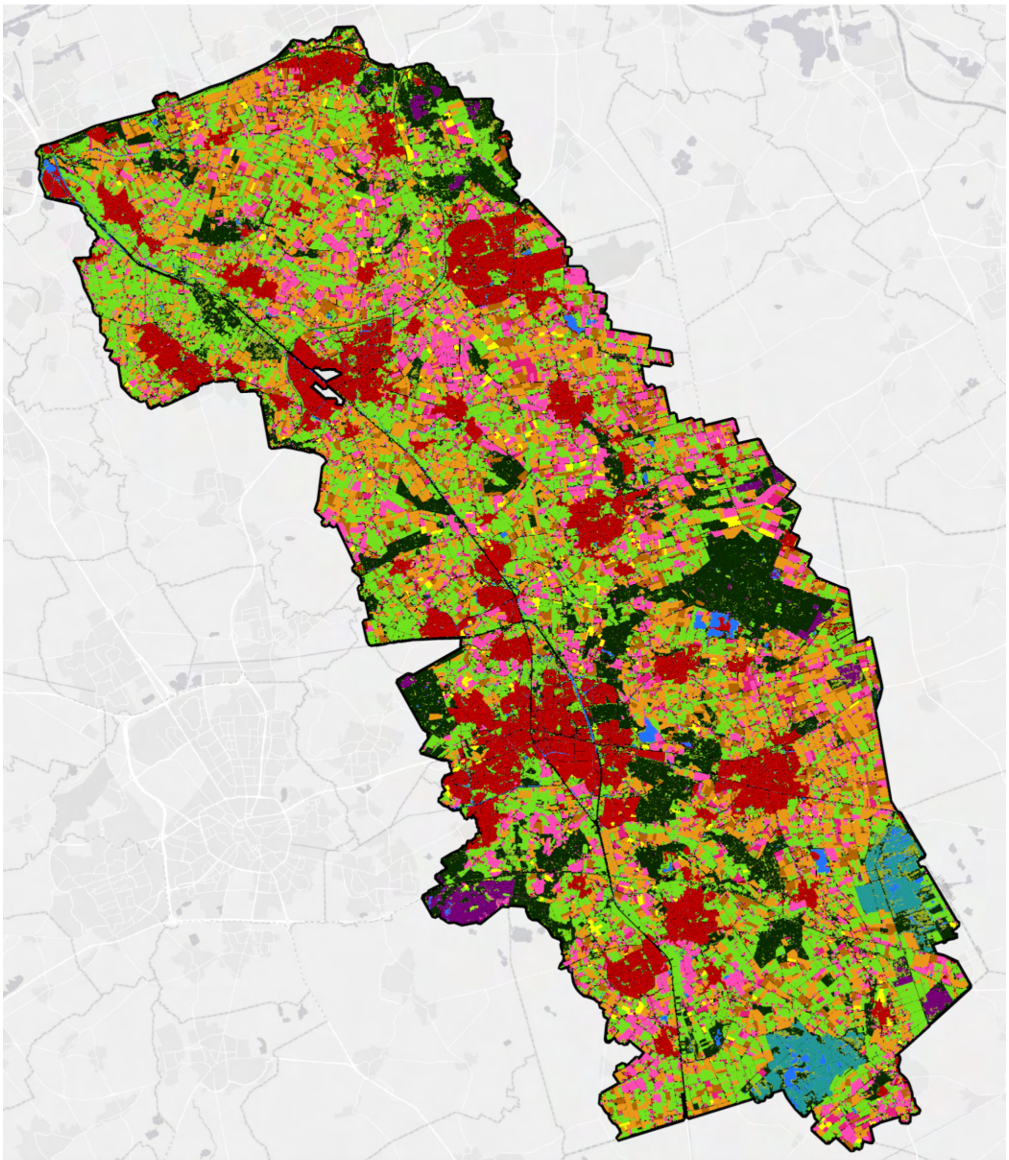

(c) Aa catchment

(d) Legend land use

Figure .7: Land use

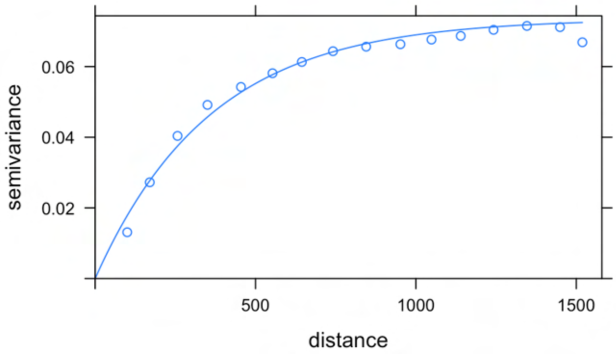

(a) Average ET_{RS}, Hupsel Brook

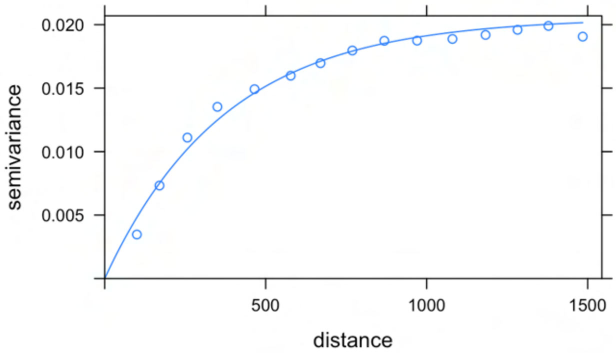

(b) Standard deviation of ET_{RS}, Hupsel Brook

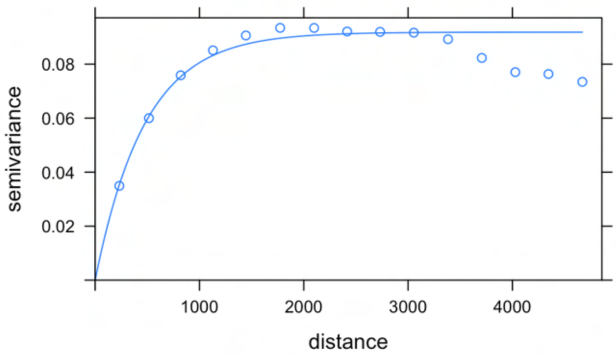

(c) Average ET_{RS}, Grote Waterleiding

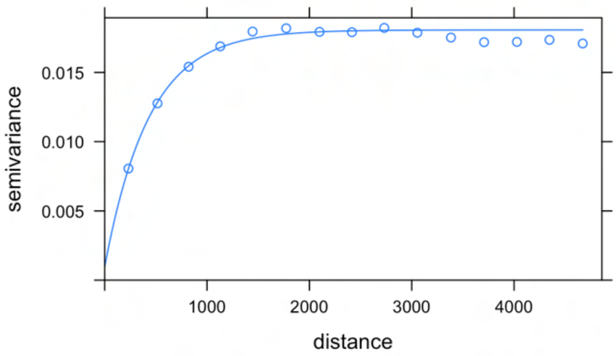

(d) Standard deviation of ET_{RS}, Grote Waterleiding

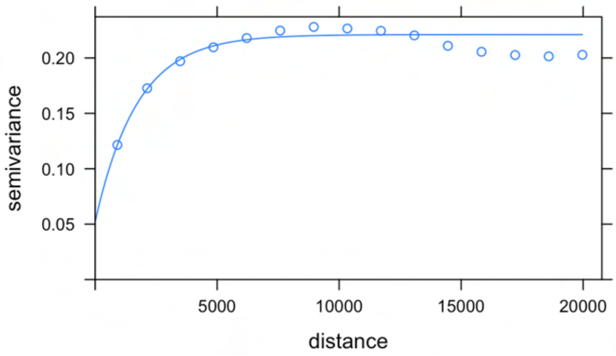

(e) Average ET_{RS}, Aa

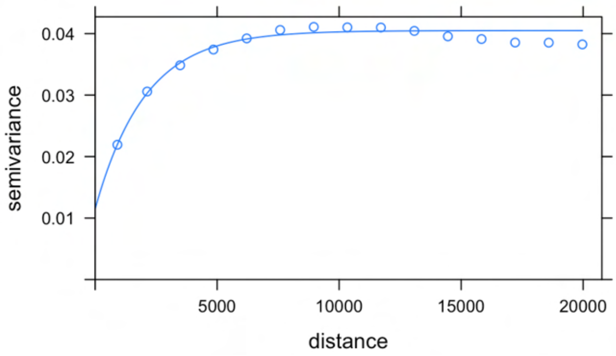

(f) Standard deviation of ET_{RS}, Aa

Figure .8: Experimental semivariogram and fitted exponential semivariogram model of average (a, c & e) and standard deviation (b, d & f) of ET_{RS} for the Hupsel Brook (a, b), Grote Waterleiding (c, d) and Aa (e, f) catchment

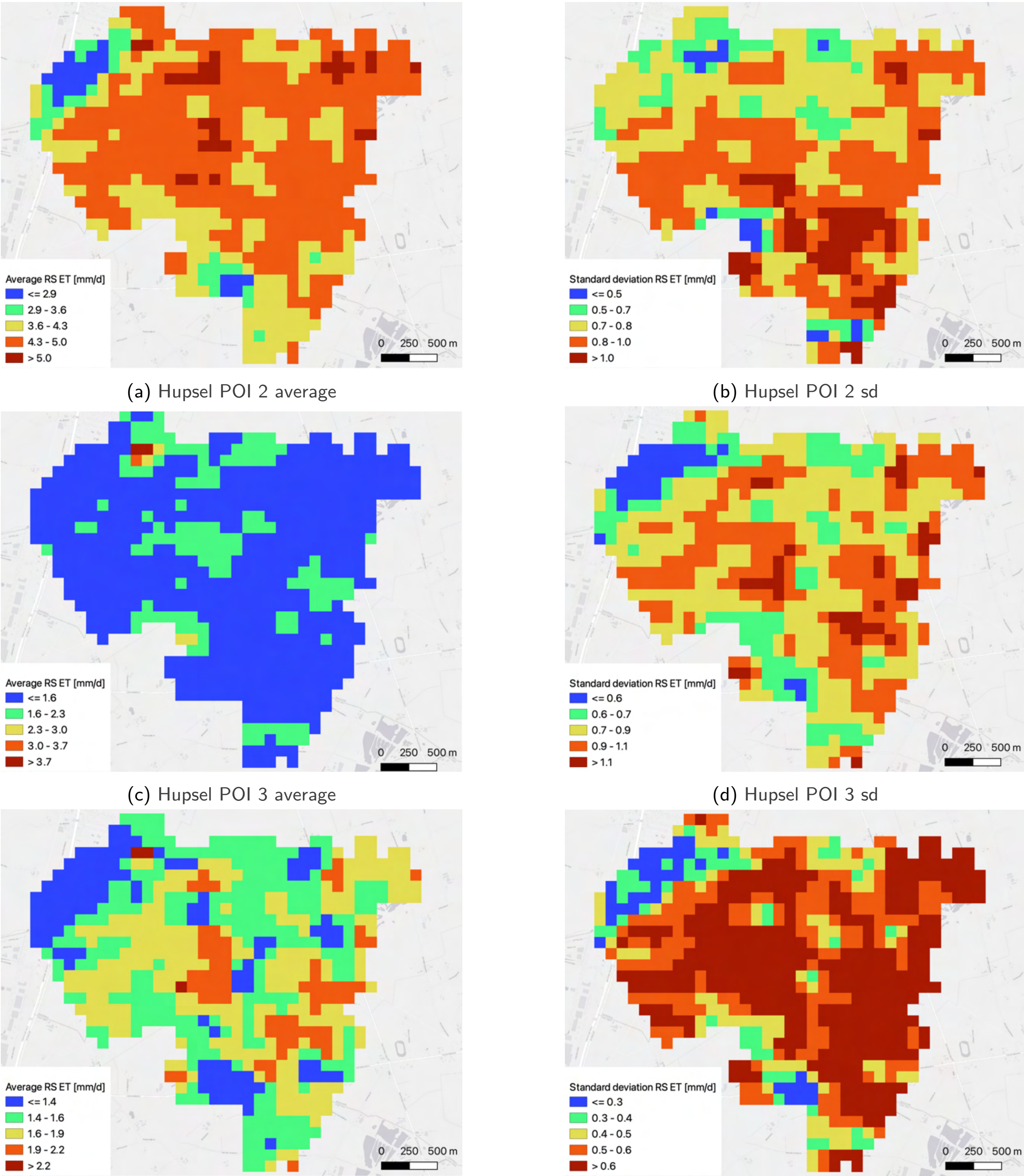

(a) Hupsel POI 2 average

(b) Hupsel POI 2 sd

(c) Hupsel POI 3 average

(d) Hupsel POI 3 sd

(e) Hupsel POI 4 average

(f) Hupsel POI 4 sd

Figure .9: Hupsel POI average and sd